

DAMAGE DETECTION IN DIRECT METAL LASER SINTERED PARTS USING
VIBRATION MODE SHAPES

A thesis presented to the faculty of the Graduate School of
Western Carolina University in partial fulfillment of the requirements
for the degree of Master of Science and Technology

By

James Philip Walker

Advisor: Dr. Sudhir Kaul
School of Engineering and Technology

Committee Members:
Dr. Wesley Stone, School of Engineering and Technology
Dr. Patrick Gardner, The Rapid Center

May 2019

ACKNOWLEDGEMENTS

I would like to thank Mom and Dad for always supporting me. I would also like to thank my advisor Dr. Kaul, I would not have finished without him. Additionally, I would like to thank my committee Dr. Gardner and Dr. Stone, the Rapid Center, as well as the faculty and my fellow students that helped me along the way.

TABLE OF CONTENTS

Table of Contents	iii
List of Figures.....	v
List of Tables.....	vii
Chapter One: Introduction	1
1.1: Introduction to Damage Detection and DMLS.....	1
1.2: Scope of Thesis	3
1.3: Overview of Thesis	4
Chapter Two: Literature Review	6
2.1 Additive Manufacturing.....	6
2.2: Direct Metal Laser Sintering (DMLS)	7
2.3: Damage Diagnostics	8
2.3.1: Laser Doppler Vibrometry.....	8
2.3.2: Natural Frequencies and Mode Shapes for Damage Diagnostics	9
2.4: Finite Element Structural Analysis	10
2.4.1: Finite Element Analysis	10
2.5: Conclusions	10
Chapter Three: Mathematical Model	12
3.1: Beam Model.....	12
3.1.1: Natural Frequency	14
3.1.2: ANSYS Simulation.....	15
3.2: Build Parameters	21
3.2.1: Build Preparation	21
3.2.2: Build Parameter Selection	22
3.3: Damage Analysis Tools	25
3.3.1 Curvature Damage Index.....	25
3.3.1 Wavelets.....	26
3.4: Conclusion	28
Chapter Four: Experimental Results	29
4.1: Experimental Setup.....	29
4.1.1: DMLS Machine (EOS M290) Setup.....	29
4.1.2: Laser Vibrometer Setup.....	31
4.2: Test Results	36
4.2.1: Detecting Natural Frequencies	36

4.2.2: Mode Shape Analysis	44
4.2.3: Build Parameters and Damage Detection.....	61
4.3: Conclusions	64
Chapter Five: Conclusions and Future Scope.....	66
5.1: Summary:.....	66
5.2: Conclusions:	67
5.3: Future Scope:	71
References.....	73
Appendix A: Example Beam Results.....	75
Appendix B: Example Matlab Code.....	95

LIST OF FIGURES

Figure 3-1: Un-Notched Beam Geometry	13
Figure 3-2: Notched Beam Geometry	13
Figure 3-3: Notched Beam First Bending Mode Shape	16
Figure 3-4: Un-Notched Beam First Bending Mode Shape	17
Figure 3-5: Notched Beam Second Bending Mode Shape	18
Figure 3-6: Un-Notched Beam Second Bending Mode Shape	18
Figure 3-7: Notched Beam Third Bending Mode Shape	19
Figure 3-8: Un-Notched Beam Third Bending Mode Shape	20
Figure 3-9: Un-Notched Beam with Added Pins	22
Figure 3-10: Un-Pinned (above) and Pinned (below) Beams	22
Figure 3-11: Sample CWT MATLAB Code	27
Figure 4-1: EOS M290 Direct Metal Laser Sintering Machine	29
Figure 4-2: Laser Vibrometer Scanning Head (right) and Vibration Generator (left)	32
Figure 4-3: Vibration Amplifier (bottom) and Amplifier Power Supply (top)	33
Figure 4-4: Beam Fixture	34
Figure 4-5: Laser Vibrometer Frequency Settings	35
Figure 4-6: Laser Vibrometer Scan Points	35
Figure 4-7: Frequency Response - Example	37
Figure 4-8: Frequency Band Selection	38
Figure 4-9: Frequency Band Peaks	38
Figure 4-10: Frequency Band with Noise Interference	39
Figure 4-11: Frequency Band Peaks with Interference	39
Figure 4-12: PSV-Displacement Results for 3rd Frequency Band	42
Figure 4-13: ANSYS Simulation Notched Geometry Mode 3	43
Figure 4-14: MATLAB Data Normalizing - Example	46
Figure 4-15: Beam N1 Bending Mode 1	47
Figure 4-16: Beam N1 Bending Mode 2	47
Figure 4-17: Beam N1 Bending Mode 3	48
Figure 4-18: U1 CODS MATLAB Code	49
Figure 4-19: Beam N1 Mode 1 CODS	49
Figure 4-20: Beam N1 Mode 2 CODS	50
Figure 4-21: Beam N1 Mode 3 CODS	50
Figure 4-22: CDI MATLAB Code	52
Figure 4-23: Beam N1 Mode 1 CDI	53
Figure 4-24: Beam N1 Mode 2 CDI	53
Figure 4-25: Beam N1 Mode 3 CDI	54
Figure 4-26: Beam N1 Mode 1 CWT	58
Figure 4-27: Beam N1 Mode 2 CWT	59
Figure 4-28: Beam N1 Mode 3 CWT	59
Figure 4-29: Beam N10 Mode 2 CDI	63
Figure 4-30: Beam N15 Mode 2 CDI	63
Figure 4-31: Beam N20 Mode 2 CDI	64

Figure A-1: Beam U1 Frequency Response.....	75
Figure A-2: Beam N1 Frequency Response.....	75
Figure A-3: Beam N10 Frequency Response.....	76
Figure A-4: Beam N15 Frequency Response.....	76
Figure A-5: Beam N20 Frequency Response.....	76
Figure A-6: Beam N10 Mode 1 Displacement.....	77
Figure A-7: Beam N10 Mode 2 Displacement.....	77
Figure A-8: Beam N10 Mode 3 Displacement.....	78
Figure A-9: Beam N10 Mode 1 CODS.....	78
Figure A-10: Beam N10 Mode 2 CODS.....	79
Figure A-11: Beam N10 Mode 3 CODS.....	79
Figure A-12: Beam N10 Mode 1 CDI.....	80
Figure A-13: Beam N10 Mode 2 CDI.....	80
Figure A-14: Beam N10 Mode 3 CDI.....	81
Figure A-15: Beam N10 Mode 1 CWT.....	81
Figure A-16: Beam N10 Mode 2 CWT.....	82
Figure A-17: Beam N10 Mode 3 CWT.....	82
Figure A-18: Beam N15 Mode 1 Displacement.....	83
Figure A-19: Beam N15 Mode 2 Displacement.....	83
Figure A-20: Beam N15 Mode 3 Displacement.....	84
Figure A-21: Beam N15 Mode 1 CODS.....	84
Figure A-22: Beam N15 Mode 2 CODS.....	85
Figure A-23: Beam N15 Mode 3 CODS.....	85
Figure A-24: Beam N15 Mode 1 CDI.....	86
Figure A-25: Beam N15 Mode 2 CDI.....	86
Figure A-26: Beam N15 Mode 3 CDI.....	87
Figure A-27: Beam N15 Mode 1 CWT.....	87
Figure A-28: Beam N15 Mode 2 CWT.....	88
Figure A-29: Beam N15 Mode 3 CWT.....	88
Figure A-30: Beam N20 Mode 1 Displacement.....	89
Figure A-31: Beam N20 Mode 2 Displacement.....	89
Figure A-32: Beam N20 Mode 3 Displacement.....	90
Figure A-33: Beam N20 Mode 1 CODS.....	90
Figure A-34: Beam N20 Mode 2 CODS.....	91
Figure A-35: Beam N20 Mode 3 CODS.....	91
Figure A-36: Beam N20 Mode 1 CDI.....	92
Figure A-37: Beam N20 Mode 2 CDI.....	92
Figure A-38: Beam N20 Mode 3 CDI.....	93
Figure A-39: Beam N20 Mode 1 CWT.....	93
Figure A-40: Beam N20 Mode 2 CWT.....	94
Figure A-41: Beam N20 Mode 3 CWT.....	94

LIST OF TABLES

Table 3-1: Beam Properties	14
Table 3-2: Values of (Bnl).....	15
Table 3-3: Bending Natural Frequencies.....	15
Table 3-4: ANSYS Simulation Natural Frequencies and Maximum Deflections	16
Table 3-5: Printing Parameters	24
Table 4-1: Un-notched Natural Frequency Result Comparison.....	40
Table 4-2: Beam Bending Natural Frequencies	44
Table 4-3: N1 31.25 Hz Scan Results Displacement	45
Table 4-4: Damage Detection from CDI Results	57
Table 4-5: Damage Detection from Wavelet Results	61
Table 4-6: Beam Printing Parameters	62

ABSTRACT

DAMAGE DETECTION IN DIRECT METAL LASER SINTERED PARTS USING VIBRATION MODE SHAPES

James Philip Walker

Western Carolina University (March 2019)

Director: Dr. Paul Yanik

Direct metal laser sintering (DMLS) is an additive manufacturing process that can be used to manufacture complex parts that are difficult or impractical to produce using traditional methods. However, this relatively new technology does not have the same base of knowledge as other processes. This makes it challenging to design parts that need to be manufactured using DMLS since many aspects related to this method are not fully comprehended.

This study investigates the use of vibrational mode shapes as a possible means of detecting damage in parts that are manufactured from DMLS. Using vibration-based damage detection is a common testing technique due to the non-destructive nature of the test. The damage detection method chosen for this study involves the use of vibrational mode shape curvatures since the change in mode shape curvature has a unique pattern at the damage location. The parts that have been used for this study were printed from the EOS M 290 machine using 316L Stainless Steel. A notch is introduced into the geometry of several parts and damage is further propagated by sawing a slot at the end of the notch. A Polytec PSV-400 Laser Doppler Vibrometer has been used to identify the vibration mode shapes, these mode shapes are then

compared to the mode shapes attributed to undamaged parts. Mode shapes have been analyzed using the wavelet transform as well as a curvature damage index.

This study also investigates the possible effect of varying part densities on damage propagation. The properties of DMLS parts that increase cost efficiency and productivity, such as layer thickness and hatch distance, inversely affect the density of parts. Damaged parts are printed with varying process parameters and the mode shapes of damaged parts are compared to one another as well as the undamaged parts.

The questions that this study seeks to answer are: Can damage of DMLS parts be detected from the mode shapes measured with a laser vibrometer? Can these mode shapes be used to predict or locate damage in parts? Do mode shapes of damaged parts differ with process parameters associated with the selective laser sintering process?

Results indicate that damage can be successfully detected in the parts analyzed in this study. Additionally, it is observed that other unknown anomalies that are similar to damage can also be successfully detected. However, varying process parameters do not seem to exhibit any influence on damage detection.

CHAPTER ONE: INTRODUCTION

1.1: Introduction to Damage Detection and DMLS

Quality control is a critical component in modern industry. Controlling the quality of each part and component is essential to ensure the safety of end users, the reliability of products, the useful life of products, reduction of scrap rates, and reduction of waste. To ensure a high level of quality and safety during operations, damage diagnostics is becoming a necessary part of testing and inspection processes during the useful life of a product. This is all the more important in large structural applications where the life cycle is long and the operating environment is rugged.

Detecting damage can be difficult for several reasons. For example, damage may be present on a micro scale that cannot be detected visually. Further, many testing methods, such as fatigue testing, are destructive and require the day-to-day operations to be stopped so that the part can be tested. This limits the usefulness of the test because it is very challenging to test every part while it is in operation. When using this type of test, it is possible to create a sampling plan to gather data on the quality of a process; however, it is possible for damaged parts to slip through untested.

Non-destructive testing, such as vibration testing using a doppler laser vibrometer, allows a 100% sample rate and the test does not require stopping operations to conduct testing. A testing method that does not destroy a sample has another key advantage over destructive testing: non-destructive testing can test for damage in components and parts that are actively in use. This capability is useful for monitoring and detecting damage early in high stress, high use, and functionally critical

components. For example, structural components of aircraft frames can be monitored for damage, allowing parts to be replaced before the damage propagate, therefore mitigating the risk of failure.

Vibrational mode shapes have already been proven as effective methods to detect and localize damage in components manufactured with traditional methods [1]. In recent years, however, the relatively new process of Direct Metal Laser Sintering (DMLS), sometimes also known as Selective Laser Melting (SLM), has begun to take the place of traditional methods, such as machining, for suitable applications. DMLS is an additive manufacturing process, also known as the 3D printing process. This method enables geometry to be constructed from layers of metal powder starting with the bottom layer and ending with the top layer. Once a thin layer of powder is deposited, a high-power laser beam melts the powder to fuse the particles in the desired layer geometry. After a layer is completed, the build plate lowers and the next layer of material is deposited and sintered.

This trend in manufacturing is due to the advantage of producing DMLS parts. These advantages include the ability to manufacture parts with complex internal features that would otherwise not be possible with traditional methods [2]. Additionally, since the building material include materials such as stainless steel and titanium, DMLS parts possess similar properties to traditionally manufactured parts and can be used for production parts.

DMLS process is a relatively new technology and does not have the same base of knowledge as traditional manufacturing methods. This study investigates the way damage manifests itself in parts manufactured by DMLS using the non-destructive

testing method by comparing vibrational mode shapes. This thesis hypothesizes that damage in DMLS parts can be detected with a laser vibrometer in a similar fashion to traditional parts.

Since DMLS is a relatively new process, many aspects of this process are not fully comprehended. Current production methods are still preferred in many production environments because the DMLS process lacks cost efficiency and productivity [2]. The metal powder used in the DMLS process is more expensive than traditional stock metal materials. Furthermore, current DMLS machinery is vastly more expensive than computer numerical control (CNC) milling machines and lathes and the additive manufacturing process often takes longer than subtractive manufacturing processes such as machining. The properties of DMLS parts that increase cost efficiency and productivity, such as laser hatching distance and layer thickness, inversely affect the density of the part. This study investigates these effects on part densities by evaluating damage, evaluated by using the vibrational mode shapes that are collected from laser vibrometry.

1.2: Scope of Thesis

The scope of this thesis includes testing cantilever beams at the first three bending mode shapes to detect damage. For this study, no other structures or mode shapes were investigated. Additionally, the damage induced in the parts consisted of a notch located in the center of the damaged beams. No other types of damage were intentionally introduced to the beams. The printing parameters considered as variables in the printing process were only the parameters that could be directly changed by the user as part of the build preparation process.

This thesis seeks to answer the following research questions:

1. Can damage of DMLS parts be detected from the mode shapes measured with a laser vibrometer?
2. Can these mode shapes be used to predict or locate damage in parts?
3. Do mode shapes of damaged parts exhibit different characteristics based on parameters associated with the DMLS process?

1.3: Overview of Thesis

The body of this thesis begins with Chapter Two. This chapter consists of a literature review to provide a frame of reference for the study. The history and processes of additive manufacturing is discussed as well as non-destructive testing. Additionally, this chapter discusses some of the tools that were used to analyze the data generated during testing.

Chapter Three, discusses the mathematical and physical models that govern this study. This includes natural frequency and mode shape models as well as FEA and 3d models of the beams that were printed. This chapter also discusses the printing parameters that were used to print the beams and why these parameters were chosen. The chapter concludes by discussing the analytical tools that were used to detect damage in the beams.

Chapter Four describes the experimental results of the study. First, the experimental setup is discussed including the DMLS build process and beam preparation. Next, the laser vibrometer test is discussed including test settings and post

processing of the results. Finally, the results are analyzed using the tools discussed in the previous chapter.

Chapter Five is the final chapter and discusses the conclusions and future scope. This chapter re-addresses the research questions posed in the introduction and explains what the results of the study mean. The future scope includes how the study can be improved as well as the next steps that can be taken to continue the research. After this chapter, there are two appendices of example results and MATLAB code.

CHAPTER TWO: LITERATURE REVIEW

This chapter provides an overview of the literature related to this study. The relevant literature provides contextual information about the research and the content of this study. The first two sections discuss additive manufacturing and DMLS and the remaining sections discuss the literature related to damage diagnostics and structural analysis.

2.1 Additive Manufacturing

Additive manufacturing (AM) is defined as a process of joining materials to make objects from a 3D model layer by layer [3]. This method of “adding” material in layers is opposed to removing material by traditional methods such as machining, milling, etc. otherwise known as “subtractive manufacturing” (SM). AM possesses several unique advantages over traditional SM processes. Firstly, AM processes have the potential to build complex shapes and interior features that can’t be built by traditional SM operations. This can be accomplished without increasing fabrication cost. Secondly, AM processes are capable of fabricating parts with multiple materials simultaneously. Thirdly, AM processes eliminate the need for tooling and manufacturing preparation time [4].

AM technology can be traced back to the mid-1980s with the introduction of stereolithography (STL) [5]. STL can be defined as “a vat photopolymerization process used to produce parts from photopolymer materials in a liquid state using one or more lasers to selectively cure to a predetermined thickness and harden the material into shape layer upon layer” [3]. Since the advent of STL, AM has expanded into seven

categories that can be categorized into three types of techniques. These techniques are stereolithography (STL), selective laser sintering (SLS), and fused deposition modeling (FDM). The STL process involves a photopolymer resin that is solidified by a UV laser. The laser follows the layer geometry solidifying the layer before the build platform is lowered and the process begins again. SLS is a powder-based process where a laser sinters the powdered material layer-by-layer to form the 3d geometry. FDM involves semi liquid material extruding from a nozzle that is deposited layer-by-layer to form the geometry [6]. AM technologies can be used for a wide range of applications and industries. Current AM technologies are used to manufacture both physical parts as well as for electronic circuit printing. Future AM technologies will be able to print fully-functional devices [7].

2.2: Direct Metal Laser Sintering (DMLS)

DMLS is an additive manufacturing technique that is used to fuse thin layers of metal powders [8]. DMLS operates by depositing a layer of powder on the build platform and then melting the powder into the geometry of the part through exposure to an infrared laser. Once a layer is complete, the build platform lowers by one layer height and a new coat of powder is applied for the next layer [9]. This technology is capable of printing parts in a wide range of materials including titanium and cobalt chrome.

DMLS can produce complicated interior features that could not be produced by using traditional manufacturing methods without sacrificing performance. However, current DMLS processes lag traditional methods with issues such as lack of cost efficiency and productivity [2]. Certain parameters of the DMLS that vary the density are directly related to cost and productivity. These parameters include layer thickness, or

how much powder metal is applied before each laser scan, and hatch distance, the distance between each pass of the laser.

Due to the nature of the DMLS process, there is the potential for parts to become damaged during the build. To deposit a new layer of material, a re-coater blade is dragged across the reservoir of fresh powder and across the build platform to dispense material. Since the process relies on high temperatures to sinter the powder, the part can become heated enough to cause excessive thermal expansion. In this case, the re-coater blade may collide with the part causing a deformation. This may lead to a failure in the build process or the part may continue to build, although with a defect at the collision location. If the next layer sinters over this defect there is the potential the build will be successful with no visual evidence of a defect.

2.3: Damage Diagnostics

2.3.1: Laser Doppler Vibrometry

Laser Doppler Vibrometry (LDV) is a method that measures the vibration characteristics of a structure through a non-contact technique. The basis of LDV is the detection of the Doppler frequency shift that occurs when light is scattered by a moving surface [10]. The sample to be tested is fixtured to a vibration generator and measured across the surface with the LDV.

LDV testing is a non-destructive testing method. Non-destructive testing is any test that does not destroy the sample to gather measurements. Non-destructive testing is capable of damage assessment in critical structural systems such as aircraft, bridges, and offshore platforms that are in use. This means that damage can be detected and repaired before catastrophic structural failure [11].

2.3.2: Natural Frequencies and Mode Shapes for Damage Diagnostics

Natural frequencies and mode shapes describe how a structure naturally vibrates. These values are directly related to the eigenvalues and eigenvectors of the system [12]. A mode of vibration and the natural frequency associated with it can be described as two waves of equal amplitude and wavelength traveling in opposite directions between two bounded ends of a structure. Once the structures meet, there is a combination of waves of equal amplitudes traveling in opposite directions. The frequency of the wave is a natural frequency of the structure and the shape of the wave is a mode of vibration, or mode shape [13]. In summary, the natural frequency of a structure is the frequency at which a structure will vibrate naturally when perturbed and allowed to vibrate freely.

The mode shape is the shape of the structure during vibration at the corresponding natural frequency. Natural frequencies shift as a structure experiences damage; however, the shift is very small for initial stages of damage. This makes the use of natural frequency for damage detection less appealing since a substantial reduction in natural frequency happens when it is too late, e.g. a part or structure fails. Mode shapes instead have been observed in the literature to be useful for damage detection in the early stages of damage. Additionally, the issues of detecting and locating damage must be addressed as separate issues. This is because a detection method that excels at identifying damage does not necessarily excel at locating the damage [14].

2.4: Finite Element Structural Analysis

ANSYS is a finite element analysis software that can be used to model and analyze structures for static and dynamic analysis. The software is capable of modeling complex structures with real-world constraints [15]. ANSYS can be used to perform finite element analysis (FEA) and calculate natural frequencies and vibration mode shapes.

2.4.1: Finite Element Analysis

FEA is a simulation process that discretizes a geometry into several small sections called elements [16]. Merriam-Webster defines finite as “having definite or definable limits” [17]. In FEA, the number of elements is fixed and known, as opposed to a model composed of infinite elements.

The advantages of FEA are that complex structures can be accurately represented including dissimilar material properties, external forces effects, and an accurate representation of the total solution [18]. FEA methods can be used to analyze a wide range of structural and nonstructural problems. These can include vibration analysis, buckling, impacts, heat transfer, fluid flow, and more [19].

2.5: Conclusions

Additive manufacturing is becoming a well-established tool in the industry. However, direct metal laser sintering is a relatively new form of additive manufacturing that uses metal powder to build parts. Furthermore, there is active research into applications that could use additive manufacturing for production and not just for making prototypes.

Non-destructive test methods can be used to inspect parts without damaging them, which is useful for production parts or parts currently in use. Inspecting vibration mode shapes is a common type of non-destructive test and the laser vibrometer allows a non-contact method that can be used for inspecting mode shapes while the part is operational and without damaging the part in any way.

CHAPTER THREE: MATHEMATICAL MODEL

This chapter discusses the theoretical background and the mathematical model that has been used in this study. The model has been used to determine the beam geometry, material, and boundary conditions that can be eventually used to finalize the test set up. The model is also used to compare the simulation results with the actual test results. The main purpose of the model is to calculate the mode shapes and natural frequencies that are measured with the PSV-400 scanning laser vibrometer during testing.

3.1: Beam Model

The beam geometry of the test samples is based on several constraints. A simple geometry is desired to make calculations and simulations as simple as possible. Furthermore, there are constraints associated with the test set up as well as the build tray used to manufacture the parts. To accommodate all the constraints, a beam with dimensions of 8in x 1in x 0.125in was selected. For damaged parts, a notch was placed at the center of the length for the damaged beam. In order to accommodate the test fixture, an additional inch was added to one end of the beam for fixturing so as to prevent the reduction of the effective length of the beam during testing. Both beams were modeled using Creo Parametric 3.0. Figure 3-1 and Figure 3-2 show the geometry of the unnotched and notched beams.



Figure 3-1: Un-Notched Beam Geometry

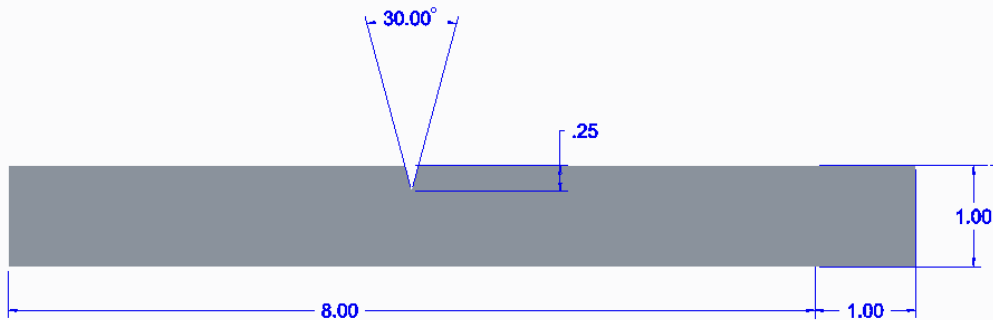


Figure 3-2: Notched Beam Geometry

The material selected for manufacturing the beams was 316L Stainless Steel. This material was chosen due to easy availability as well as the usage of this material. 316L is a widely-used material in aviation and medical applications, as well as other

industries. Additionally, the EOS M290 DMLS used for making parts for this study is already prepared to run 316L Stainless Steel as the build material.

In order to calculate the natural frequencies and bending mode shapes of the geometries selected, the properties are listed in Table 3-1. The end conditions of the beam are considered as a fixed-free, or cantilever, configuration.

Table 3-1: Beam Properties

Property	Value	Units
Modulus of Elasticity (E)	193	GPa
Inertia (I)	6.7204×10^{-3}	m^4
Density (ρ)	7980	kg/m^2
Area (A)	8.0645×10^{-2}	m^2

3.1.1: Natural Frequency

Once the beam geometry and conditions are selected, the natural frequencies can be calculated as follows:

$$\omega_n = (B_n l)^2 \sqrt{\frac{EI}{\rho A l^4}} \quad (1)$$

In Eq. (1), $B_n l$ is a constant, E is the modulus of elasticity, I is the inertia, ρ is the density, and A is the area of the beam. For a cantilever beam, the first three ($B_n l$) values for bending modes can be found in Table 3-2 [20], the remaining variables in the equation can be found in Table 3-1.

Table 3-2: Values of $(B_n l)$ for First Three Bending Modes

$(B_1 l)$	1.875104
$(B_2 l)$	4.694091
$(B_3 l)$	7.854757

Using the natural frequency equation from Eq.(1) and the values listed in Table 3-1 and Table 3-2, the first three bending natural frequencies have been calculated, these results can be found in Table 3-3.

Table 3-3: Bending Natural Frequencies for First Three Bending Modes

ω_1	54.768 Hz
ω_2	343.227 Hz
ω_3	961.046 Hz

It may be noted that additional modes, such as longitudinal and torsional, may be identified during testing. This will be discussed further in subsequent sections.

3.1.2: ANSYS Simulation

An alternate method has been used to identify the natural frequencies and modes. Finite element analysis is a numerical method that can be used to model the unnotched as well as the notched beam. A finite element analysis software, ANSYS, has been used to find the first ten natural frequencies and mode shapes. For this

simulation, a modal analysis was conducted using the Block Lanczos mode extraction method [21] . Of these ten modes, only the first three bending modes were considered for this model and are listed in Table 3-4.

Table 3-4: ANSYS Simulation Natural Frequencies and Maximum Deflections

	Notched		Unnotched	
Bending Mode	Frequency	Max Deflection	Frequency	Max Deflection
Shape	(Hz)	(mm)	(Hz)	(mm)
1	61.3525	5.55442	61.536	5.54
2	380.418	5.50859	385.145	5.53993
3	1076.46	5.63257	1077.68	5.54822

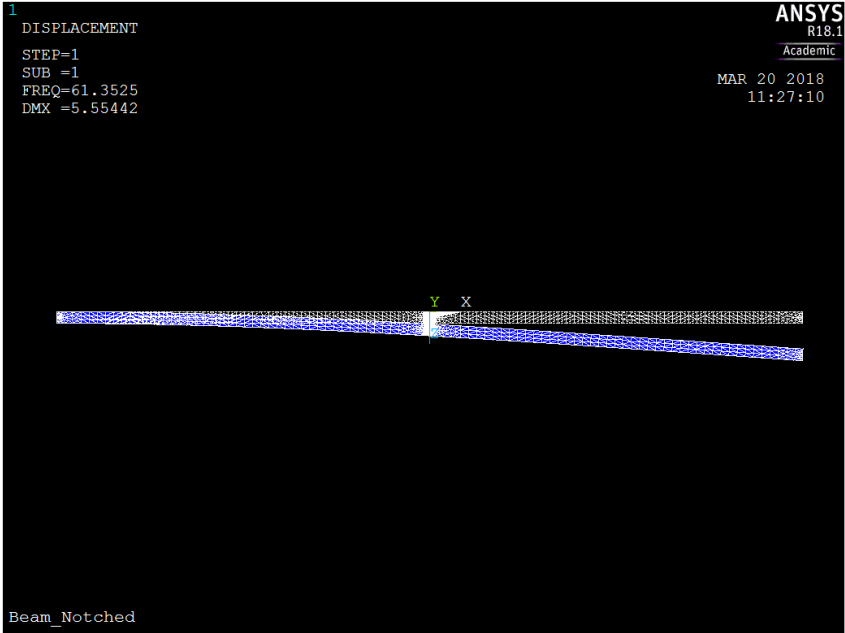


Figure 3-3: Notched Beam First Bending Mode Shape

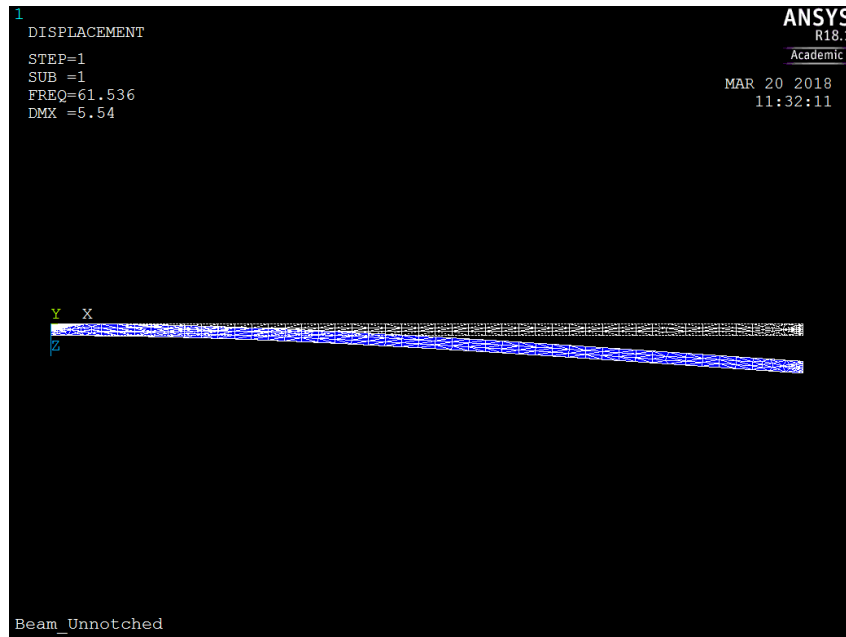


Figure 3-4: Un-Notched Beam First Bending Mode Shape

Figures 3-3 and 3-4 depict the ANSYS solution for the first bending mode shape of a notched (Figure 3-3) and an un-notched (Figure 3-4) beam. The figures feature a depiction of the beam before deflection in grey and then the maximum deflection of the beam in blue. The natural frequencies and maximum deflections found by ANSYS in these simulations are tabulated above in Table 3-4.

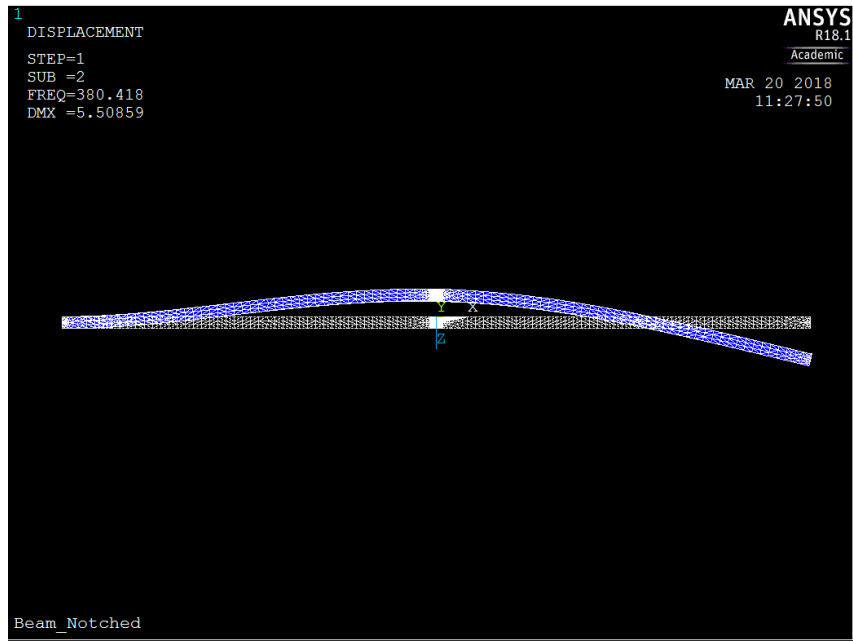


Figure 3-5: Notched Beam Second Bending Mode Shape

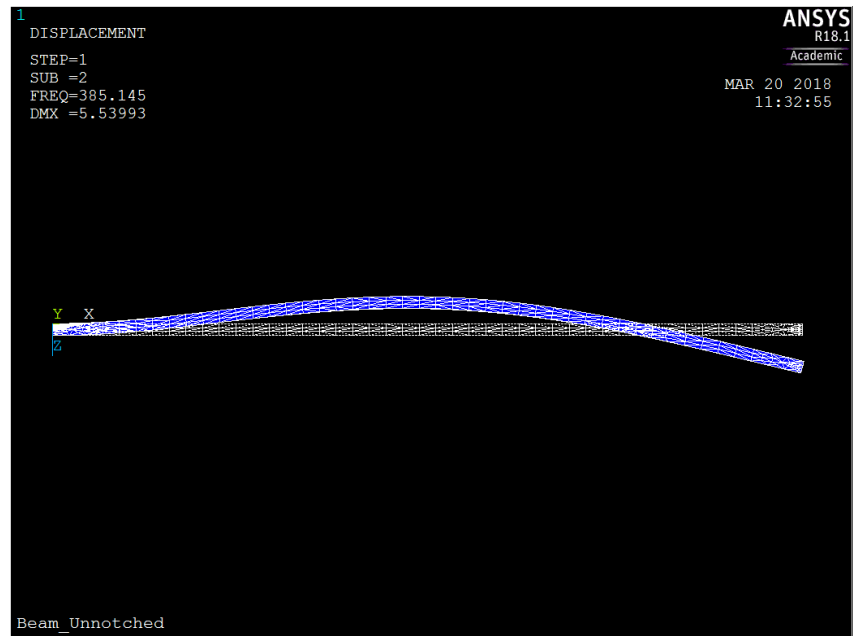


Figure 3-6: Un-Notched Beam Second Bending Mode Shape

Figures 3-5 and 3-6 depict the ANSYS solution for the second bending mode shape of a notched (Figure 3-5) and un-notched (Figure 3-6) beam. This mode shape is particularly interesting because the maximum deflection is located at the notch location, the center of the beam. This mode shape also has an additional node where the curve crosses zero towards the right end of the beam.

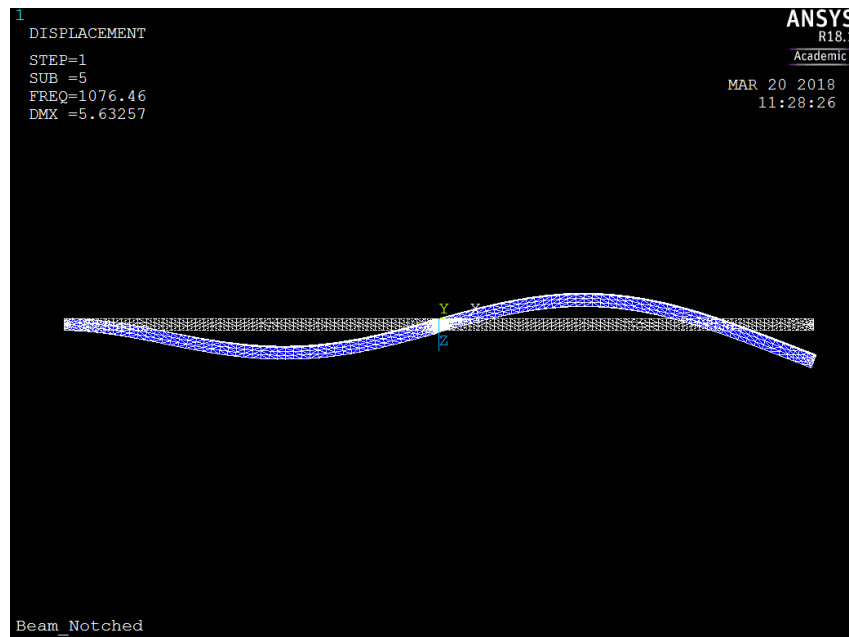


Figure 3-7: Notched Beam Third Bending Mode Shape

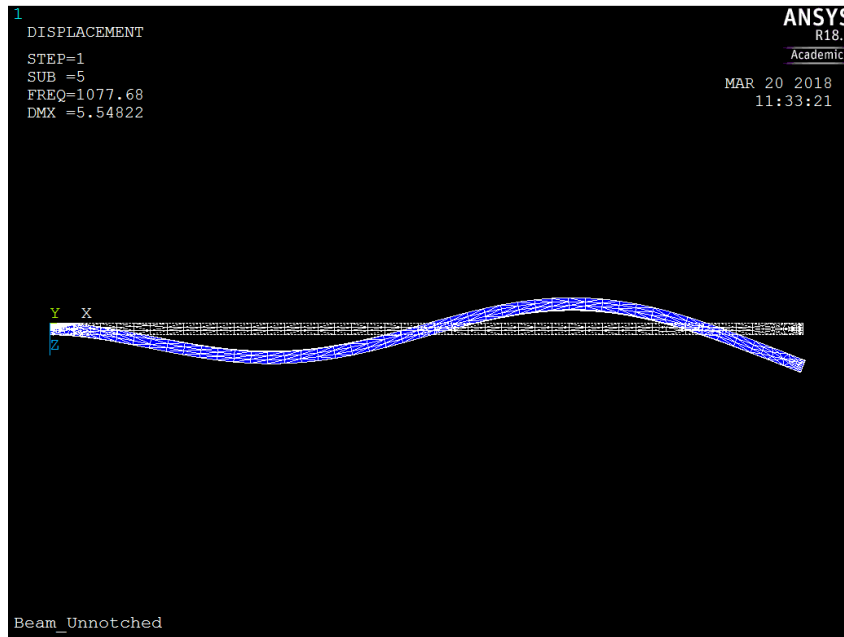


Figure 3-8: Un-Notched Beam Third Bending Mode Shape

Figures 3-7 and 3-8 depict the ANSYS solution for the third bending mode shape of a notched (Figure 3-7) and an un-notched (Figure 3-8) beam. For this mode, there is a node present right at the location of damage at the center of the beam. This means that there will be very little, if any, deflection at the notch for this mode. This has the potential to mask any dissimilarities between the notched and the un-notched beam.

Since ANSYS found these solutions using numerical methods, they do not exactly match the solution from the closed form solution. However, the ANSYS solutions are still useful to verify the results that are measured with the laser vibrometer. These results can be compared with the analytical results found in Table 3-3 and will be discussed in the next chapter.

3.2: Build Parameters

3.2.1: Build Preparation

Some preparation is required before starting the build on the EOS M290 machine. The geometrical modeled from Creo 3.0 is used to prepare a STL file by using Materialise Magics (Version 22). Within Materialise Magics, the STL files are checked for errors including overlapping triangles, multiple shells, and other commonly found errors. Once any errors are corrected, appropriate support material can be generated to assist the build.

Initially, the beams were printed as designed in Figure 1-1 and Figure 1-2. However, upon removing these beams from the build platform it was discovered that the edges of the beams delaminated from the build platform and bent upwards. Additionally, the top surface of the beams sagged downward at the center.

To overcome these problems, three pins were added to the beam design. The un-notched, pinned model is shown in Figure 3-9. The same three pins were added to the notched model as well. A pin was added at each end of the beam to hold the ends of the beam securely to the build platform. A pin was also added to the center of the beam as a support to prevent the center section of the beams from sagging. These pins were machined away after printing. An example of an un-pinned beam whose edges delaminated from the build platform and a pinned beam with the pins machined away can be found in Figure 3-10.

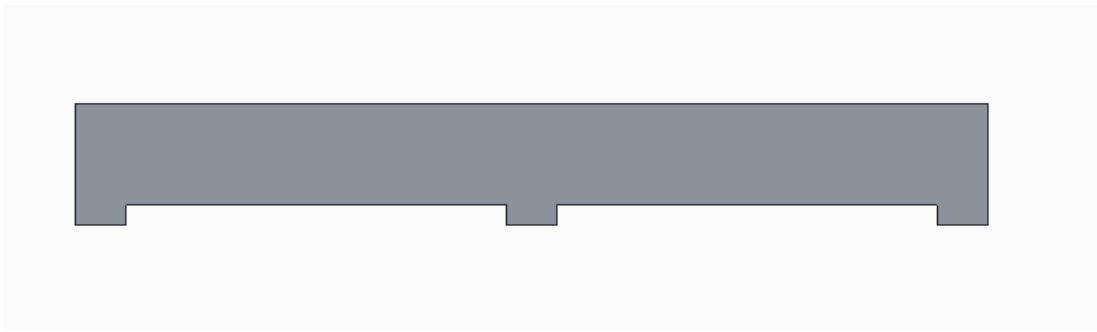


Figure 3-9: Un-Notched Beam with Added Pins



Figure 3-10: Un-Pinned (above) and Pinned (below) Beams

3.2.2: Build Parameter Selection

Selecting proper building parameters is critical for a successful print. The DMLS process considers four main parameters: laser power, scan speed, layer thickness, and hatch distance. Laser power is a measure of the intensity of the scanning laser beam. This parameter is limited by the maximum power of the laser in EOS M290. The laser has a maximum power of 400W, however the M290 limits the power to 370W.

Scan speed is a measure of how fast the laser moves across the powder bed during the build process. Combined, scan speed and laser power determine the quality of the melt pool. The more powerful the laser setting, the faster the scan speed should be to compensate. If the power is too high and the scan speed too low, the laser may burn away too much powder into condensate, as a result the metal powder that evaporates can re-solidify in the build chamber and create a porous finish.

Layer thickness is a measure of how much powder is applied for each layer during the build process. This parameter is interesting because prints with fewer layers print faster. This is because the machine must apply additional layers of powder. Each time the machine adds layers there are several steps it must complete. These steps begin with lowering the build plate and the dispenser platform out of the way to move the re-coater blade back to the starting position. Next, the build plate and dispenser platform are moved back into position and the re-coater blade must move across the build platform to deposit material. All these steps add time to the build process.

The final parameter is hatch distance. This parameter controls how close each laser pass is to the neighboring passes. The smaller the hatch distance, the more passes the laser will take to complete a layer.

When selecting build parameters, the clear starting point is to use EOS default print parameters. These parameter sets are the settings that are recommended by EOS with EOS Print 2.0 for each machine and material set, and have proven to generate quality prints. These parameters were used for the un-notched beams as well as the first set of notched beams. These beams have been used as the benchmark to which

the other parameter sets are compared. Layer thickness and hatch distance have been chosen as the two parameters that will be varied for this study.

Changing printing parameters can have drastic effects on the quality of a print and can even cause a print to fail within the first few layers of the build process. Energy density is the value that is used to measure the level of energy per unit volume that is input into a part. Maintaining a suitable energy density is critical for a successful print.

The equation for energy density is defined as:

$$E = \frac{P}{v \cdot h \cdot t} \quad (2)$$

In Eq. (2), P is laser power (W), v is scan speed (mm/s), h is hatch spacing (mm), and t is layer thickness (mm) [22]. Using Eq. (2), the parameter sets were identified and are listed Table 3-5.

Table 3-5: Printing Parameters

	Parameters	
Level	Hatch Distance (mm)	Layer Thickness (mm)
High	0.12	0.04
Low	0.09	0.02

3.3: Damage Analysis Tools

One of the main goals of this study is to investigate means of identifying damage. Therefore, once the natural frequencies and mode shapes of each beam are calculated, analytical tools must be chosen to take the data points and compare the damaged data with the undamaged data. This is critical because simply comparing mode shapes and natural frequencies manually is a time-consuming process even when considering a small number of scan points. Larger structures, for example a large truss member in a bridge, may require many scan points and the need to manually investigate each point severely limits the usefulness of a damage detection method.

Additionally, part to part variation combined with potentially miniscule damage could easily mask damage locations when the mode shapes are compared manually. For these reasons, two analytical tools have been chosen to detect damage in this study. These techniques are the curvature damage index and the continuous wavelet transform.

3.3.1 Curvature Damage Index

The curvature damage index (CDI) is a tool that compares the vibrational response of two structures to identify any differences in the response. When comparing two identical structures, these differences could highlight any variation that may be resulting from damage. Since the CDI is a measure of differences between two structures, abrupt anomalies in structural integrity are more visible in the results of this technique.

The first step in creating the CDI is to calculate the curvature of operating deflection shape (CODS) of each structure. CODS uses a variation of the central difference method to create a curve of the mode shapes generated from the data collected from the laser vibrometer scans. CODS can be calculated as:

$$y''(x) = \frac{y(x-h) - 2y(x) + y(x+h)}{h^2} \quad (3)$$

In Eq. (3), $y''(x)$ is the CODS of the structure, $y(x)$ represents each scan point generated from the vibrometer scan, and h is the distance between each scan point. The value, h , determines the resolution of the ODS. Increasing the number of scan points increases the resolution, however it will also increase the time taken to complete the scan [23].

Once the CODS is calculated for each beam, the CDI can be used to determine the differences between the beams. In this study, the differences between undamaged and damaged beams have been found by using the above-discussed approach. CDI can be computed as follows:

$$\Psi(x) = [y''_d(x) - y''_p(x)]^2 \quad (4)$$

In Eq. (4), $\Psi(x)$ is the resulting CDI that captures any differences between the two beams. The variable $y''_d(x)$ is the CODS of the damaged beam and $y''_p(x)$ is the CODS of the undamaged beam.

3.3.1 Wavelets

For each mode, a continuous wavelet transformation (CWT) is performed as an additional damage detection method. The CWT uses the data gathered from the laser vibrometer along with a mother wavelet to detect any discontinuities in the mode shape [24]. The CWT can be calculated as:

$$Wf(u, s) = [f, \Psi_{u,s}] = \frac{1}{\sqrt{s}} \int_{-\infty}^{+\infty} f(x) \Psi\left(\frac{x-u}{s}\right) dx \quad (5)$$

In Eq. (5), $Wf(u, s)$ is the wavelet coefficient of the wavelet $\Psi_{u,s}(x)$. This coefficient is used to find discontinuities by using the natural mode. The variable u is the translation parameter and s is the scale [25].

The wavelet transform has been performed by using MATLAB [23]. The db4 wavelet has been selected as the mother wavelet for this study. This wavelet has been chosen because of the high number of vanishing moments, which are critical for detecting discontinuities [26].

An example code in MATLAB that has been used to calculate the CWT can be found in Figure 3-11.

```

211 -     c1 = cwt(ydd_u_1, 1:128, 'db4');
212 -     figure
213 -     plot(c1(10, :));
214 -     title('N1 Wavelet Transform Mode 1')
215 -     grid
216 -     xlabel('Scan Points')
217 -     ylabel('Amplitude')

```

Figure 3-11: Sample CWT MATLAB Code

In Figure 3-11, Line 211 in the sample code is where the CWT is performed. The term $c1$ is the wavelet coefficient with multiple scales and ydd_u_1 is the CODS for bending mode 1. The next part of the code, 1:128, refers to the range of scales to be considered and the final section, db4, refers to the mother wavelet. In line 213, scale 10

is specified to be plotted. The scale can be adjusted from 1 to 128 until the notch positions can be detected, however in this case scale 10 has been found to work well [25] and will be discussed further in the next chapter.

3.4: Conclusion

The mathematical model presented in this section has been used to determine the test set up and, therefore, forms the basis for the analysis that is to follow. The bending natural frequencies and mode shapes have been calculated by using hand calculations as well as an ANSYS FEA simulation. These results will be used to validate the test data gathered during the laser vibrometry scans. The tools used to analyze these natural modes to identify damage include the curvature of operating deflection, curvature damage index, and the continuous wavelet transform. These techniques will be used to compare the damaged beams to undamaged beams without any notches.

CHAPTER FOUR: EXPERIMENTAL RESULTS

This chapter presents the experimental setup used for testing, this includes the testing apparatus, fixturing, and software settings. Additionally, all the analysis results are presented in this chapter with the relevant discussion.

4.1: Experimental Setup

4.1.1: DMLS Machine (EOS M290) Setup

The Direct Metal Laser Sintering (DMLS) machine used to manufacture the beams in this study was an EOS M290 with parameters suitable for 316L Stainless Steel. The default parameters are recommended by EOS and are suitable for the 316 L Stainless Steel material. The user can also choose alternative parameters for each print. The printing parameters chosen for this study and the associated factors that have been discussed in Chapter 3.



Figure 4-1: EOS M290 Direct Metal Laser Sintering Machine

Before each build, a check needs to be performed to ensure that there is enough 316L powdered metal and enough argon gas to complete the print. Since combustion is always a concern when working with powdered metal, argon gas is used to flood the build chamber to lower oxygen concentration to safe levels. Additionally, a build plate must be prepared and installed in the machine. The build plates are steel blocks that the metal powder is distributed across. These plates can be re-used, however between each use the plates must be milled flat to remove the remaining support material from previous builds. Between each build, a 6-inch 7-insert face mill was used to prepare the build plate for the subsequent build.

As discussed in Chapter 3, once the three-dimensional model of the beam is complete, it is imported into Materialise Magics (Version 22) for printing preparation. In Materialise Magics, the model is checked for common errors associated with making the STL. Once the errors are eliminated, the support material can be generated. Support material performs three functions: supporting the geometry of the part, facilitating removal of the part from the build plate, and providing a conduit for heat to flow from the part into the build plate. Basic support material geometries are included in the parameter sets purchased from EOS.

EOS Print (version 2.0) is then used to create the file that is used by the M290 machine to build the part. This involves loading the part file, including support material, that is prepared in Materialise Magics. During this step the parts are oriented on the build plate and the printing parameters can be selected for each part.

The beams are oriented on the build plate 15 degrees to soften the blow from the re-coater blade as it distributes more powder. If the parts are oriented normal to the

blade, the force of the blade could bend them, causing the build to fail. Additionally, the parts on the build platform must be far enough apart from each other to facilitate the removal of un-sintered powder when the build plate is removed from the build chamber.

Once the build is complete, un-sintered powder is removed from around the parts and the build plate is removed from the machine. To remove the parts, a horizontal bandsaw is used to cut the support material between the part and the build plate. Next, each beam was fixtured in a HAAS vf3 mill and the remaining support material was machined off. Finally, a hacksaw was used to propagate damage at the notch to manufacture damaged beams that can be used for testing. The beams were fixtured together and cut simultaneously to ensure that the damage was similar on multiple samples.

4.1.2: Laser Vibrometer Setup

The first step in generating results for the experiment carried out in this study is to measure the vibrational mode shapes. A doppler scanning laser vibrometer (Manufacturer: Polytec, Model: PSV-400) was used for this purpose. A few additional pieces of hardware, including a vibration generator and amplifier, were necessary to complete this testing.

The scanning head of the laser vibrometer is fixed to a pneumatically stabilized and isolated table. The vibration generator is also mounted on this table. The mounting plate for the vibration generator sat 43 inches away from the lens of the scanning head. An external amplifier with its own power supply was connected to the vibration generator to control the frequency and amplitude of the generated vibrations. The scanning head and the vibration generator were both controlled with the PSV

workstation. This workstation also collected and stored the data. The test setup with the scanning head and the vibration generator setup can be seen in Figure 4-1 and the vibration amplifier can be seen in Figure 4-2.

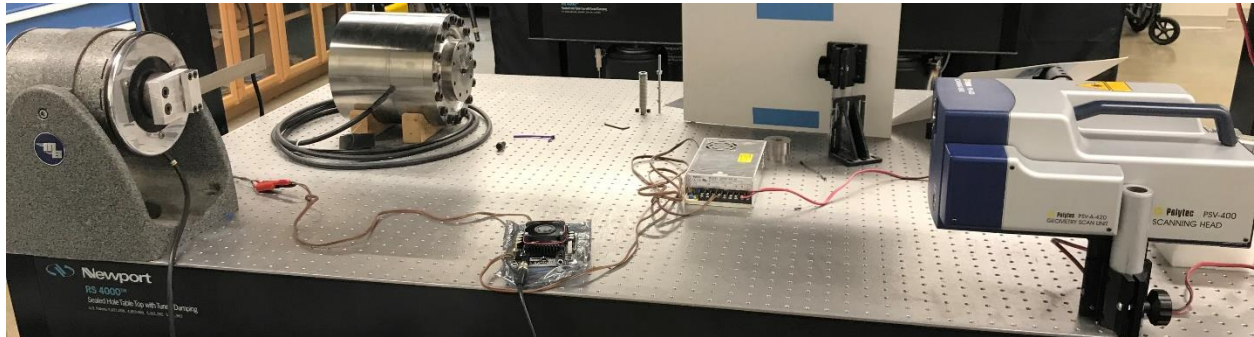


Figure 4-2: Laser Vibrometer Scanning Head (right) and Vibration Generator (left)

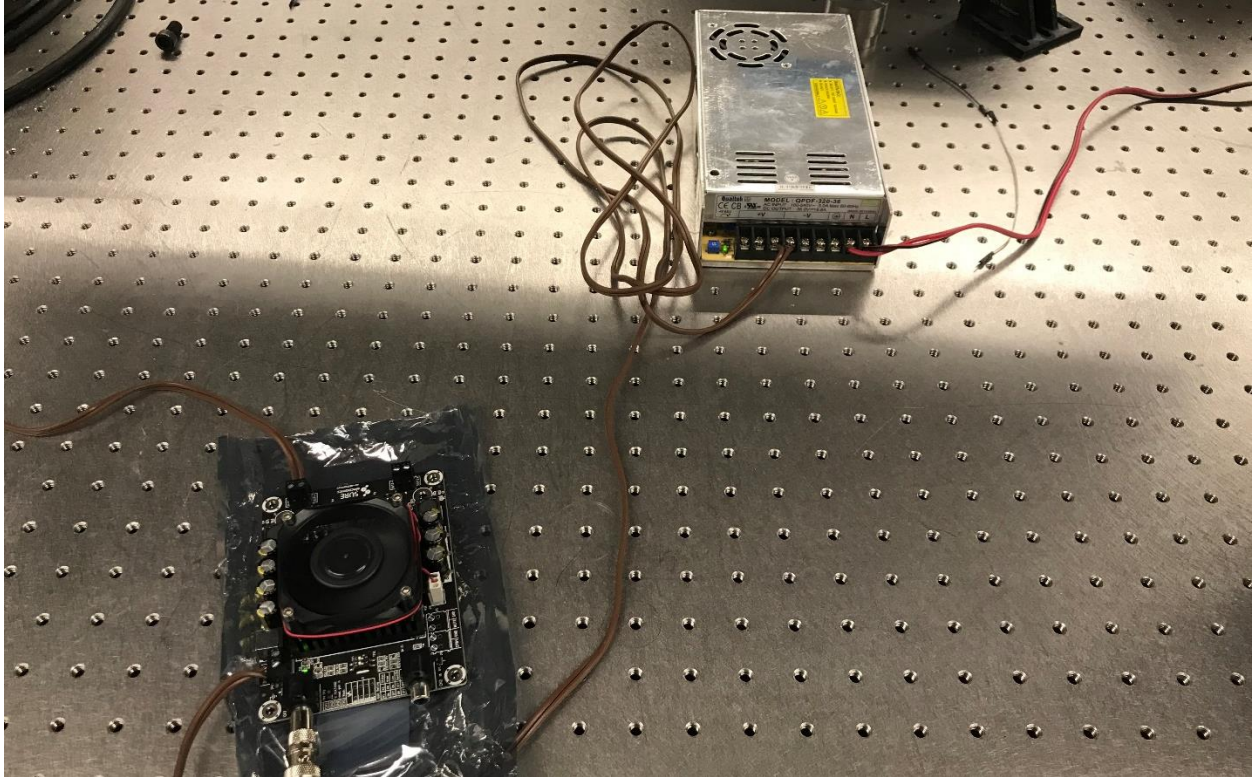


Figure 4-3: Vibration Amplifier (bottom) and Amplifier Power Supply (top)

To mount the beams to the vibration generator it was necessary to create a fixture. This fixture was machined from a block of 6061 aluminum. A slot was machined in the face to repeatedly locate the beams in the z-plane and to prevent any rotation. Each beam was inserted into the fixture flush with the end. To allow for this fixturing, an additional 1 inch of length was added to each beam as is discussed in Chapter 3. The fixture is attached to the vibration generator using 4 bolts to capture the beam between the fixture and the mounting plate, as shown in Figure 4-3.



Figure 4-4: Beam Fixture

After placing the beam in the fixture, the next step was to set the test parameters. The software used to run the vibrometer is PSV Acquisition (Version 9.2). Since the simulation results discussed in Chapter 3 indicated the frequency of the third bending mode shape to be approximately 1000 Hz, the smallest frequency setting of 10 kHz was selected by setting the scan range from 0 Hz to 10 kHz. The resolution of the scan was 3.125 Hz. This means that within the scan range the step between each frequency will be 3.125 Hz, this resolution is deemed to be sufficient for the purposes of this study. A snapshot of the settings can be seen in Figure 4-4.

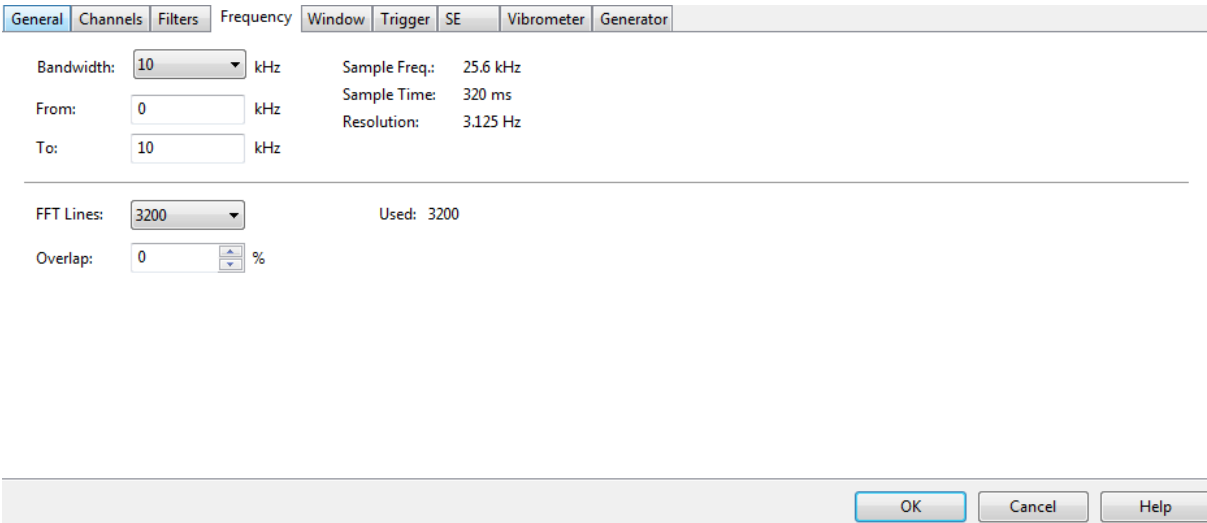


Figure 4-5: Laser Vibrometer Frequency Settings

Next, scan points at which the laser vibrometer collects data were set. For this study, a single line of scan points is considered to be sufficient. This is because the study is only investigating the bending mode shapes, which can be represented with a single line of scan points, as shown in Figure 4-5.

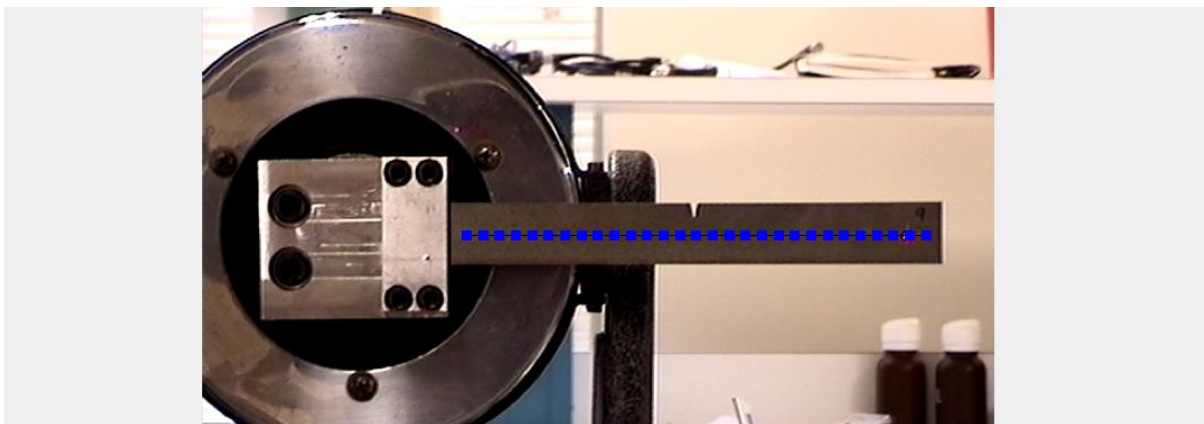


Figure 4-6: Laser Vibrometer Scan Points

Initially, 20 scan points were chosen to represent the beam. This includes one point at the base of the beam at zero length. Later, some of the beams were re-scanned with 30 scan points to enhance the analysis. Increasing point density improves the resolution of the gathered data, however it also increases scan time. Increasing scan time can be problematic in large systems since damage detection can become extremely time consuming.

The PSV-400 equipment includes several analog and digital decoders to gather data. The velocity decoder used for this test is VD-03 and the range of 100 mm/s/V has been found to be appropriate for this test. The displacement decoder used was DD-500 and a range of 5mm/V has been found to be appropriate [27].

To eliminate any background noise, a high-pass filter is used during data acquisition to limit any low frequency interference in the environment, such as climate control of the building or other noises caused by nearby equipment. The isolated stabilized table that was used for mounting was further able to isolate the test from outside vibrations.

4.2: Test Results

4.2.1: Detecting Natural Frequencies

The results from the laser vibrometer include the velocity response across the entire range of scanned frequencies, 0 Hz to 10 kHz. The velocity of each scan point is recorded for each scanned frequency. The natural frequencies can be easily located from the range of frequencies because they can be identified as local maxima. This is due to the nature of natural frequencies since these frequencies correspond to the peak response.

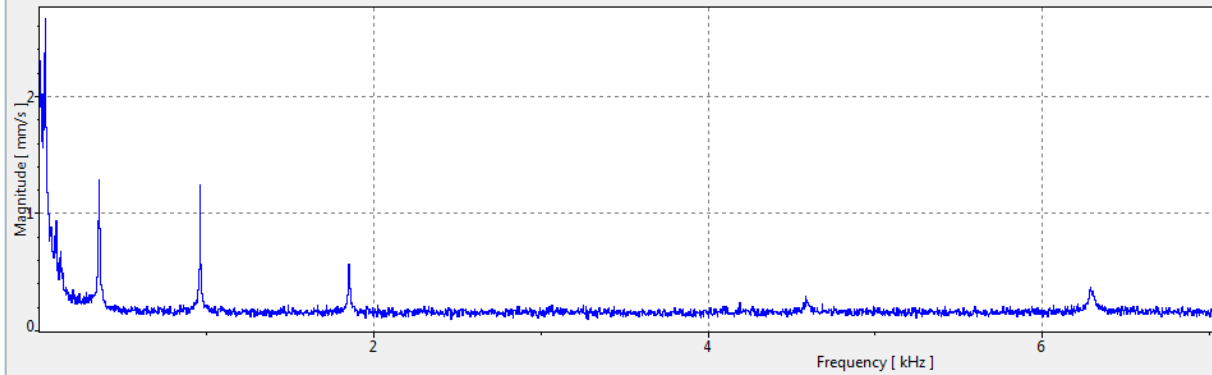


Figure 4-7: Frequency Response - Example

Figure 4-6 shows an example of the initial results from a completed vibrometry scan. The x-axis shows the frequencies, 0 Hz to 10 kHz, that the beam was subject to and the y-axis shows the magnitude of the response (velocity). The response indicates several spikes towards the lower frequencies, these spikes correspond to the first three bending natural frequencies of the beam.

To isolate these spikes, the frequency spectrum is split into three separate bands, each of which incorporates one of these magnitude spikes. The peak of each band is used to detect the corresponding natural frequency. These values can be found in the screen shot in Figure 4-7. A visual representation of the frequency bands with each maxima can be seen in Figure 4-8.

No.	Start	End	Peak	Bandwidth	Unit
1	31.25	100	34.375	68.75	Hz
2	200	800	356.25	600	Hz
3	800	1200	962.5	400	Hz

Figure 4-8: Frequency Band Selection

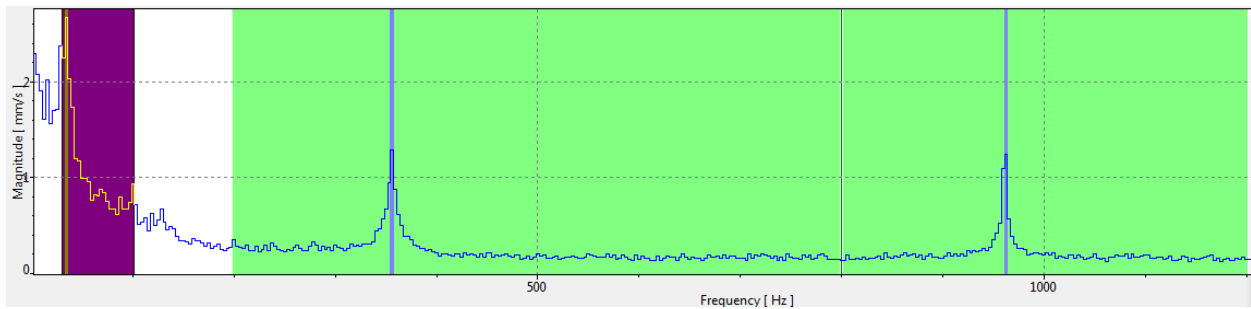


Figure 4-9: Frequency Band Peaks

The values chosen for the boundaries of each frequency band were based on several constraints. First, the frequency step of 3.125 Hz used during the scan means that only values that fall in this interval can be considered. Second, the bands must include only one of the frequency spikes. Finally, noise can interfere with locating the local maximum in the first two bands.

At the beginning of the frequency spectrum, the magnitude begins with a large spike that gradually lowers to the same baseline level that is present in the rest of the

spectrum. This spike is likely due to the higher levels of background noise experienced at the lower frequencies. This noise may include any vibrations not caused by the vibration generator. The first natural frequency is located within the end of this initial spike. Due to the proximity of this spike, if the boundaries for the first and second frequency band are not chosen carefully, the maximum calculated by the software will not correspond to the correct natural frequency. An example of this issue can be found in Figure 4-9 and Figure 4-10.

No.	Start	End	Peak	Bandwidth	Unit
1	31.25	100	34.375	68.75	Hz
2	100	800	106.25	700	Hz
3	800	1200	965.625	400	Hz

Figure 4-10: Frequency Band with Noise Interference

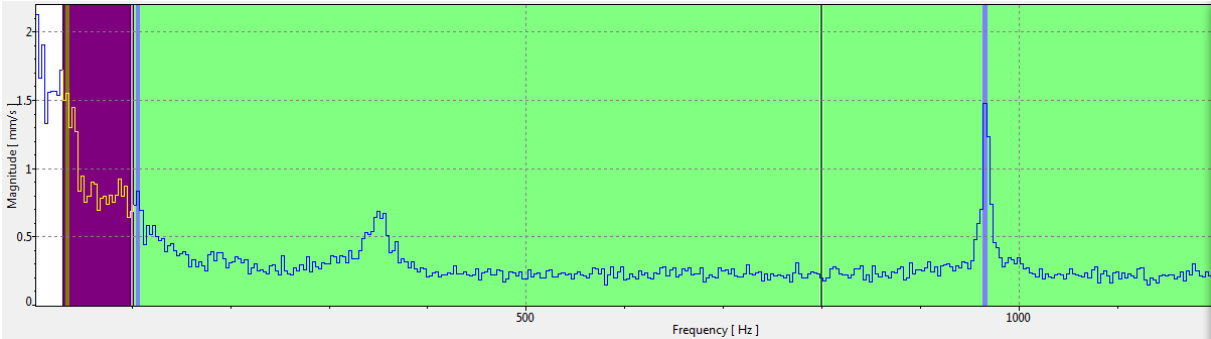


Figure 4-11: Frequency Band Peaks with Interference

In Figure 4-9, the peak of the second band appears to be located at 106.25 Hz. However, looking at Figure 4-10, it is obvious that the local maxima is located closer to 300 Hz. The maximum of 106.25 Hz that is reported in the frequency band definition is represented as a thin purple line near the pink field representing the first frequency band in Figure 4-10. Not only does the 106.25 Hz not correspond to the results anticipated in the mathematical model, visually it can be seen that this value is part of the noise spike at the beginning of the spectrum. The band can be narrowed to eliminate this noise and allow the true local maxima to be represented. An example of measured frequency results compared to the mathematical model in Chapter 3 can be found in Table 4-1.

Table 4-1: Un-notched Natural Frequency Result Comparison

Un-notched Natural Frequency Result Comparison – U1			
	1 st Bending Natural Frequency (Hz) (Un-notched)	2 nd Bending Natural Frequency (Hz) (Un-notched)	3 rd Bending Natural Frequency (Hz) (Un-notched)
Hand Calculation	54.768	343.227	961.046
ANSYS Simulation	61.536	385.145	1077.68
Measured Response	34.375	356.25	962.5

Table 4-1 demonstrates that the measured responses are within the same magnitude as the expected results except for the first frequency. The first bending natural frequency is approximately 50 Hz, the second bending natural frequency is approximately 350 Hz, and the third bending natural frequency is approximately 1000 Hz. It can be observed that as the frequency increases, the variations between the anticipated and measured results shrink.

The mode shapes corresponding to the natural frequencies can be further verified as the first three bending mods by examining the deflection profiles. Figure 4-11 shows an example of the information available from the PSV Presentation software for beam N9. The maximum displacement at each scan point can be seen at the top. This displacement can be compared to the shape in Figure 4-12 to verify that it is the correct mode shape for this frequency.

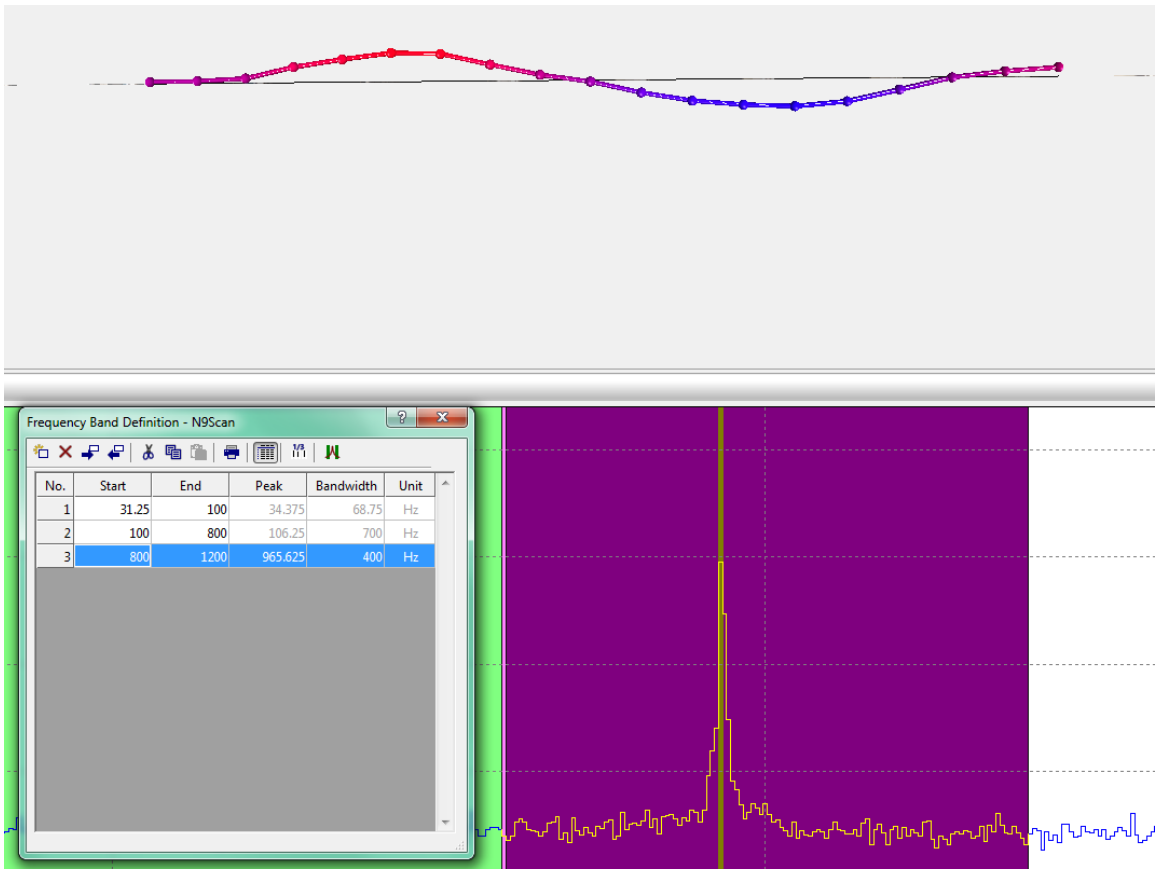


Figure 4-12: PSV-Displacement Results for 3rd Frequency Band

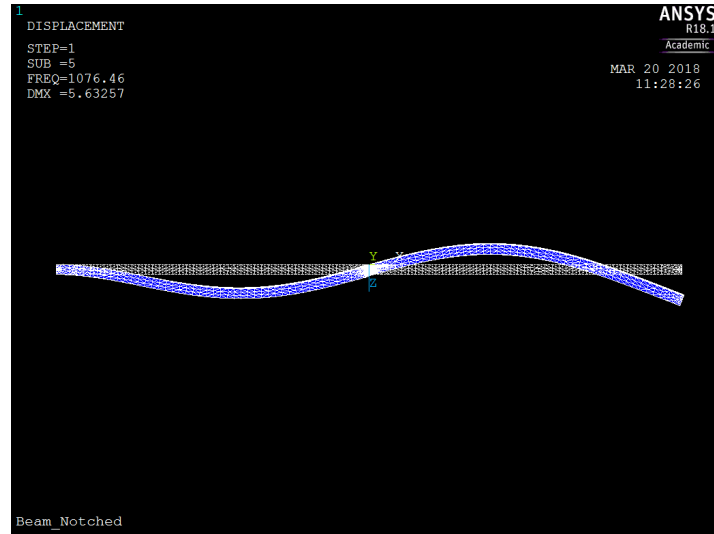


Figure 4-13: ANSYS Simulation Notched Geometry Mode 3

Table 4-2 summarizes the bending natural frequencies for each beam. Most of the frequencies for each beam match the expected results. Several beams, N4, N5, N13, N18, and N19 measured unexpected results for the second bending mode. Upon inspecting the frequency bands, it was discovered that these frequencies are the result of end effect interference. The actual value for these frequencies appears to be in line with the other results. It may be noted that the prefix 'U' has been used for un-notched beams whereas the prefix 'N' has been used for notched (or damaged) beams.

Table 4-2: Beam Bending Natural Frequencies

Beam Bending Natural Frequencies			
Beam	Mode 1 Frequency (Hz)	Mode 2 Frequency (Hz)	Mode 3 Frequency (Hz)
U1	34.375	356.25	962.5
U2	50	350	975
U3	34.375	353.125	968.75
U4	31.25	343.75	959.375
U5	31.25	346.875	968.75
N1	31.25	348.875	962.5
N2	34.375	343.75	956.25
N3	31.25	350	959.375
N4	31.25	106.25	956.25
N5	28.125	106.25	962.5
N6	31.25	356.25	984.375
N7	25	343.75	956.25
N8	46.875	350	975
N9	34.375	356.25	981.25
N10	31.25	356.375	975
N11	31.25	328.125	903.125
N12	34.375	340.625	921.875
N13	28.125	106.25	906.25
N14	34.375	331.25	909.375
N15	50	312.5	871.875
N16	31.25	340.625	943.75
N17	31.25	350	956.25
N18	46.875	106.25	940.625
N19	40.625	106.25	953.125
N20	31.25	334.375	931.25
Mean	34.625	296.96	949.625
Std. Dev.	6.668489	95.85225	27.33359

4.2.2: Mode Shape Analysis

One of the goals of this study is to compare the differences in mode shapes between damaged and un-damaged beams. At the basic level this involves analyzing the maximum displacement of each scan point and comparing these values for notched

beams against these values for un-notched beams. The results from the laser vibrometer scan tabulate the magnitude at each point for specific frequencies. For example, the results for beam N1 at 31.25 Hz can be found in Table 4-3.

Table 4-3: N1 31.25 Hz Scan Results Displacement

N1 31.25 Hz Displacement				
Index	X	Y	Z	Magnitude [m/s]
1	-0.00726	0.003418	-1	0.000778
2	0.002357	0.003494	-1	0.000954
3	0.011972	0.00357	-1	0.001211
4	0.021587	0.003646	-1	0.001408
5	0.031174	0.003708	-1	0.001465
6	0.040779	0.00378	-1	0.001458
7	0.050393	0.003855	-1	0.001376
8	0.060006	0.00393	-1	0.001219
9	0.069619	0.004005	-1	0.001249
10	0.079233	0.004081	-1	0.00128
11	0.088846	0.004156	-1	0.001227
12	0.09846	0.004231	-1	0.001095
13	0.108073	0.004306	-1	0.001035
14	0.117687	0.004381	-1	0.00099
15	0.1273	0.004457	-1	0.001007
16	0.136913	0.004532	-1	0.001057
17	0.146524	0.004606	-1	0.001101
18	0.156129	0.004676	-1	0.001394
19	0.165733	0.004747	-1	0.001638

The laser vibrometer scan yields several results at each point. The first column in Table 4-3 lists each scan point. There are 19 points considered in the scan. One more point is added later at the boundary of the beam with a magnitude of 0 m/s. The X and Y columns tabulate the position of each scan point in the global coordinate system used

by the scanning head. Since this is a 2-dimensional scan and all the points are on the same surface, the column for the z-coordinate shows the same value for every point. The final column lists the velocity magnitude measured at each point by the scanning head. These magnitudes in the final column are used for further analysis.

At this stage, MATLAB is used to analyze the data. The first step is to normalize the values. This is done by dividing each value by the maximum value, allowing the beams to be examined in relation to maximum deflection instead of absolute deflection. This will allow an easy comparison between multiple beams and detect abnormalities due to any damage. An example of the MATLAB code can be found in Figure 4-13.

```
6 - ml_vel=xlsread('N1Scan_31.25_Hz_Fixed.xlsx');  
7  
8 - ref_vel=max(abs(ml_vel));  
9  
10 - ml_vel=ml_vel/ref_vel;  
11  
12 - ml_disp=ml_vel;
```

Figure 4-14: MATLAB Data Normalizing - Example

The results of this normalization are then plotted. This plot is a representation of the mode shape of the beam. This is repeated for each natural frequency. Figure 4-13, Figure 4-14, and Figure 4-15 show these mode shapes for beam N1. Each of these mode shapes match the expected results from the ANSYS simulation.

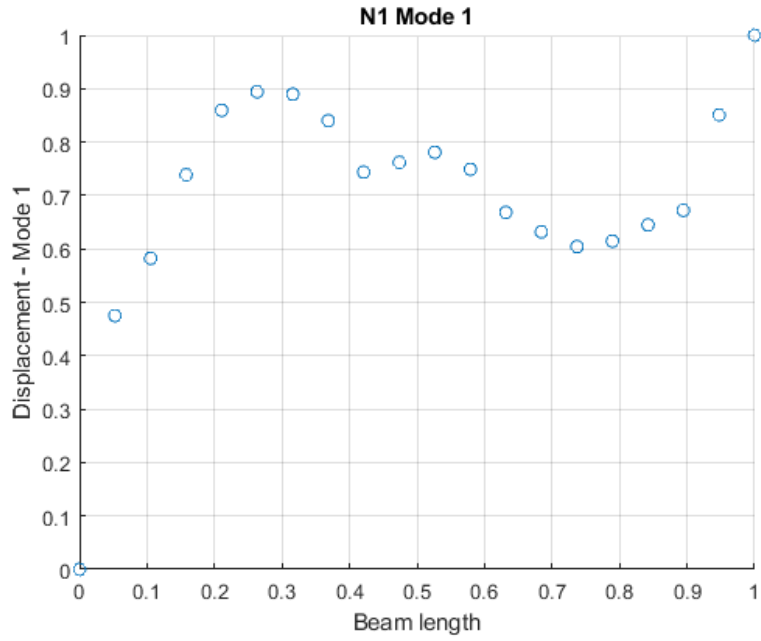


Figure 4-15: Beam N1 Bending Mode 1

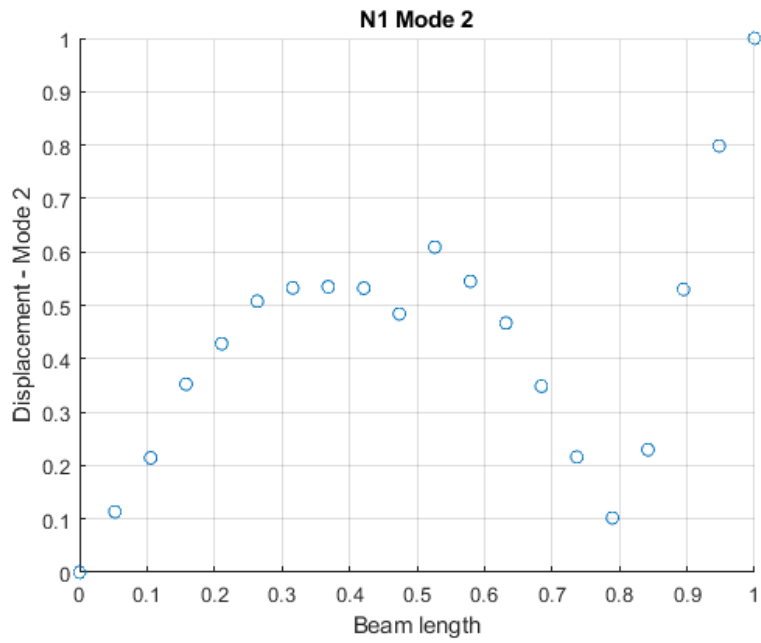


Figure 4-16: Beam N1 Bending Mode 2

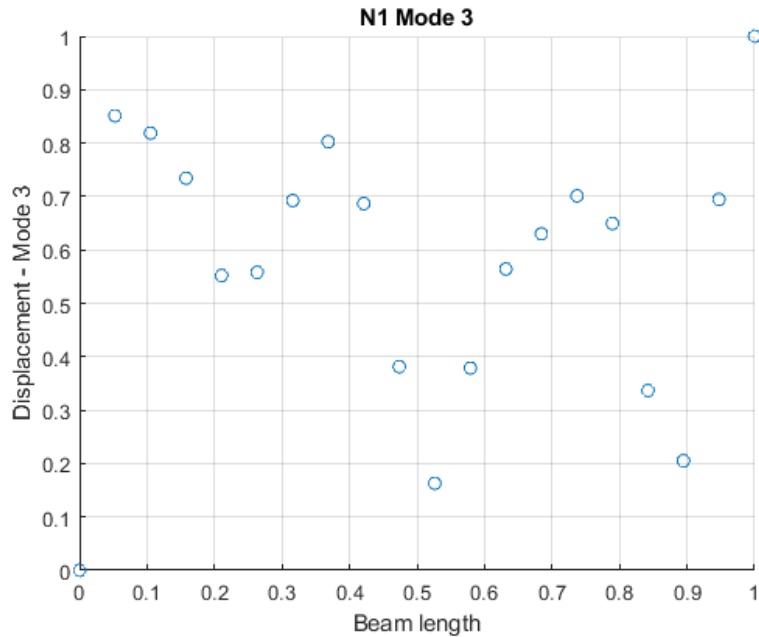


Figure 4-17: Beam N1 Bending Mode 3

This series of normalization and graphing is repeated for each beam. Comparing one beam to another using these graphs may show discrepancies in displacement, however it is difficult to draw any conclusions this way. Instead, the next step is to create a damage index.

To create the damage index, a curvature of operating deflection shape (CODS) is needed. The detailed explanation of finding the CODS can be found in Chapter 3.

Figure 4-17 depicts the MATLAB code that has been used to generate the CODS for the first mode of beam U1. In Figure 4-17, `ydd_u_1` refers to the CODS. Each CODS is also normalized so that they can be compared on the same scale. This normalization can be seen beginning on line 105 in the figure and ends on line 107 in Figure 4-17. A

graphical representation of the CODS of modes 1, 2, and 3 for Beam N1 can be found in Figure 4-18, Figure 4-19, and Figure 4-20.

```
100 % U1 CODS
101 ydd_u_1_U1=[];
102 for i = 2:1:19
103     ydd_u_1_U1=[ydd_u_1_U1 (ml_disp_U1(i-1)-2*ml_disp_U1(i)-ml_disp_U1(i+1))/h^2];
104 end
105 ydd_u_1_U1_max = max(abs(ydd_u_1_U1));
106 ydd_u_1_U1_Fixed = ydd_u_1_U1/ydd_u_1_U1_max;
107 ydd_u_1_U1=[0 ydd_u_1_U1_Fixed 0];
```

Figure 4-18: U1 CODS MATLAB Code

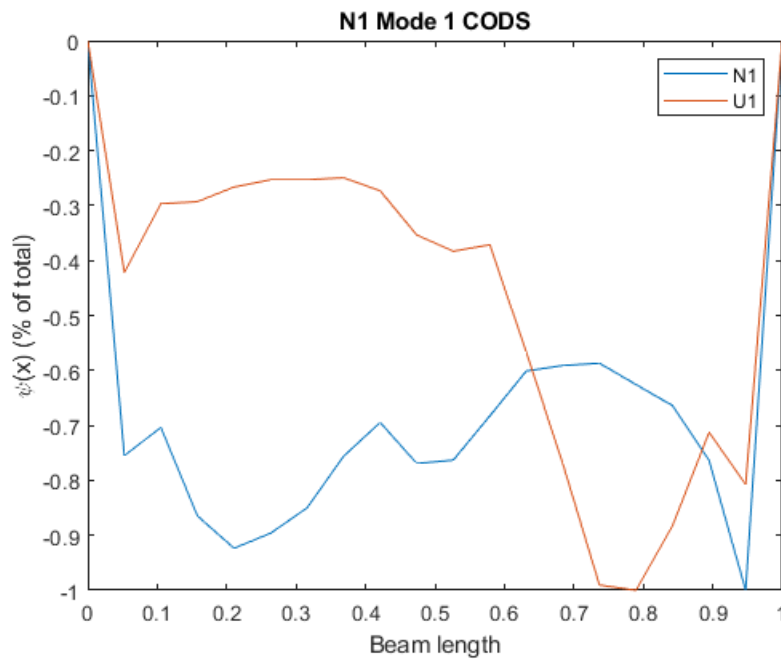


Figure 4-19: Beam N1 Mode 1 CODS

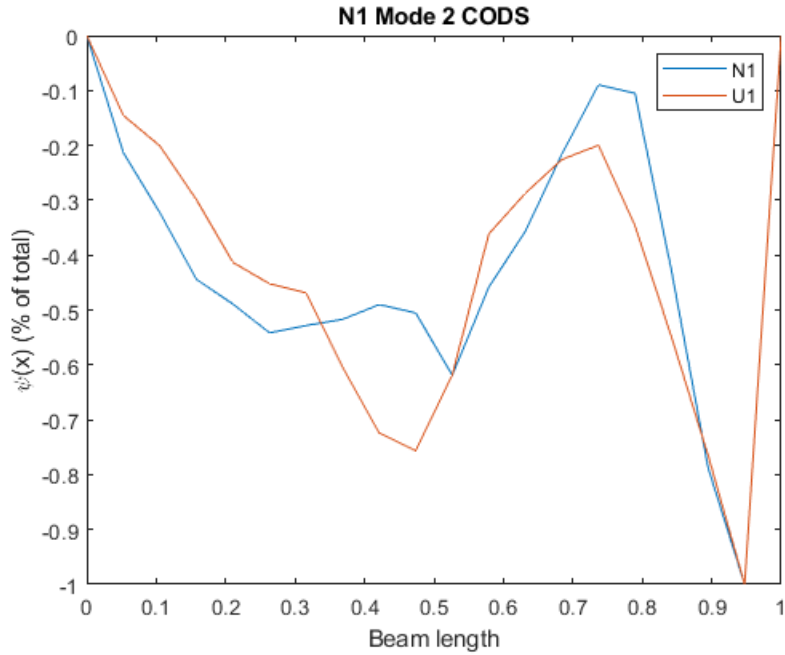


Figure 4-20: Beam N1 Mode 2 CODS

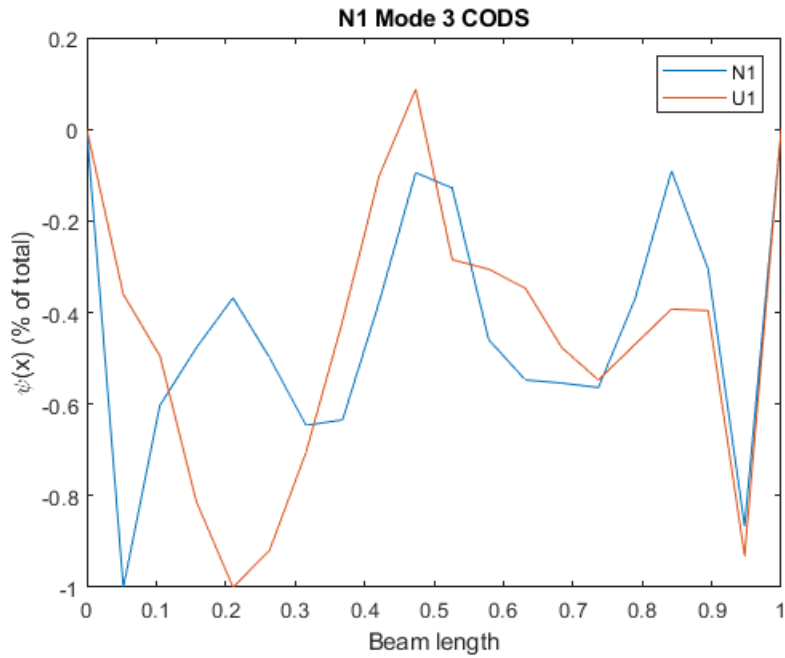


Figure 4-21: Beam N1 Mode 3 CODS

In these figures, the CODS for the un-notched geometry is represented in blue and the CODS for Beam N1 (notched beam) is represented in orange. The x-axis of the graphs is the length of the beam, this axis is unitless because the values relate to the maximum length of the beam scaled between 0 and 1. The y-axis relates to the deflection as a percentage of the maximum deflection.

At this stage, several trends begin to appear. First, the second mode shape tends to yield the clearest results with the least unexpected discontinuities. Also, the second mode shape closely matches the simulation results. It can also be noticed that there tend to be abrupt spikes and discontinuities towards the end of the beam, especially for the first mode shape.

Some of the possible causes for these trends can be explained. One cause is related to the position of nodes, or where the deflection crosses zero, on the mode shapes. The first mode shape is such that one end of the beam experiences little to no deflection while the other end experiences the maximum deflection and the corresponding natural frequency is most vulnerable to noise. The second mode shape includes one node where there is zero deflection, however, the maximum deflection occurs at the notch location. The third mode shape includes two nodes, one of which is located directly at the notch. This implies that in the first and third mode shapes, there is little to no deflection at the damage location. This indicates that the second mode could be most successful in detecting damage for the sample examined in this study.

A possible cause for the spikes and discontinuities seen in the test data at the ends of the beams could be attributed to end effects. End effect is the tendency for results to demonstrate significant spikes in the neighborhood of the boundary conditions

[28]. To limit errors due to end effects, the boundaries of the signal were padded by adding a value of zero to the beginning and the end.

The next step is to take the CODS value and create the curvature damage index (CDI). CDI involves taking the difference of two beams at each scan point and squaring the results. A detailed explanation of CDI can be found in Chapter 3 and an example of the code used in MATLAB to calculate CDI can be found in Figure 4-21. A graphical representation of the CDI for beam N1 can be found in Figure 4-22, Figure 4-23, and Figure 4-24, each figure demonstrates the CDI for each mode for the first three bending modes.

```
181 -   CDI_N1_Model = (ydd_u_1 - ydd_u_1_U1).^2;  
182 -   CDI_N1_Model_Max = max(abs(CDI_N1_Model));  
183 -   CDI_N1_Model = CDI_N1_Model/CDI_N1_Model_Max;
```

Figure 4-22: CDI MATLAB Code

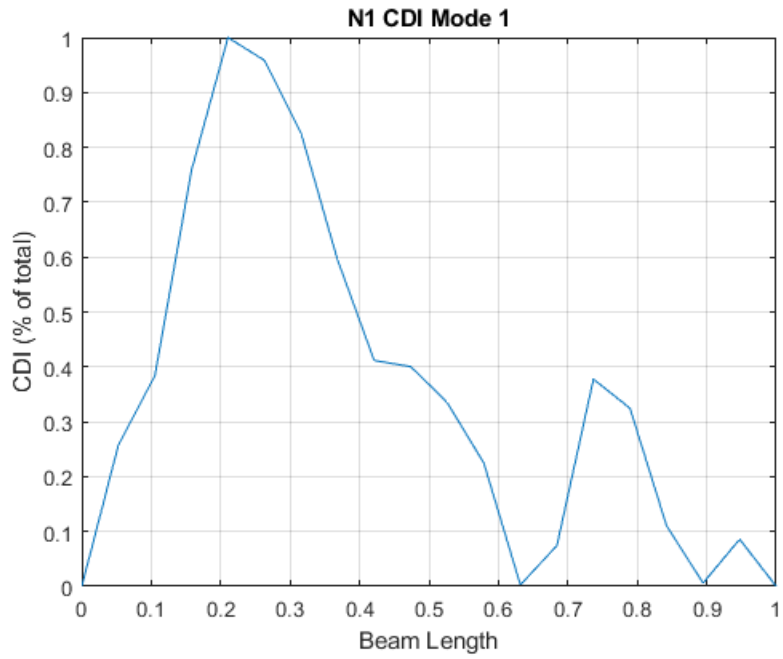


Figure 4-23: Beam N1 Mode 1 CDI

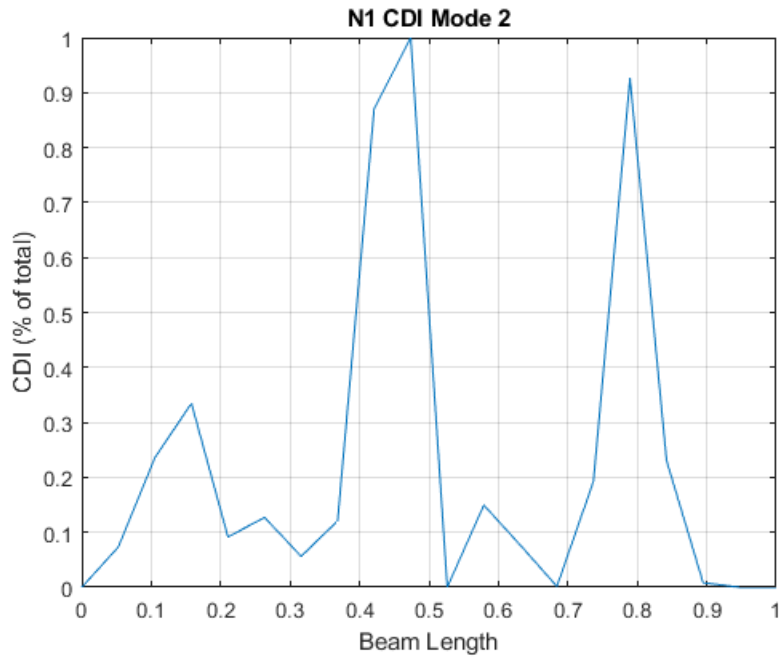


Figure 4-24: Beam N1 Mode 2 CDI

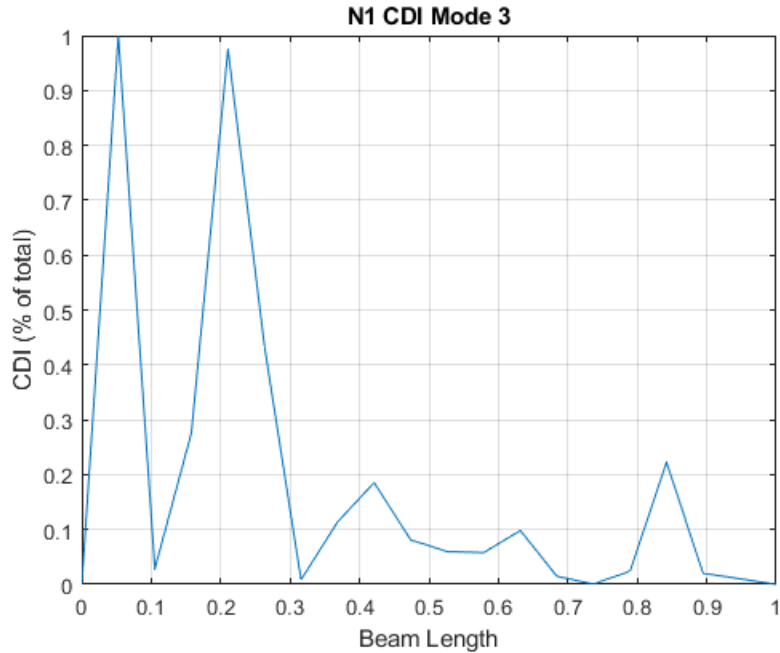


Figure 4-25: Beam N1 Mode 3 CDI

These CDI plots in Figure 4-22, Figure 4-23, and Figure 4-24 represent the differences in mode shapes between the un-notched and notched geometries. The x-axis represents the normalized length of the beam in relation to maximum length. The y-axis represents the damage index, or the difference between the mode shapes of beam N1 and beam U1, in relation to the maximum difference. Each spike on the graph correlates to a discontinuity between the notched and un-notched mode shape. For the first mode shape in Figure 4-22, it appears that the beginning of the mode shape does not match closely. However as described above, at this point of the mode shape the deflections are relatively small. Any anomalies measured by the scanning head along this section of the beam could easily lead to higher discrepancies between the beams. This is compounded by the fact that at low frequencies, such as this first mode shape,

there are higher risks of noise interference. These factors limit the usefulness of the first bending mode shape to detect damage that is not located towards the end of the beam geometry.

For the CDI of the third mode shape in Figure 4-24, there are two spikes near the beginning of the beam and a smaller spike towards the end. The notch location, at 0.5 on the x-axis, does not correlate to a noticeable spike. The lack of a spike at the notch location is likely since displacement of the beam is very low at this point for the third mode shape. The first spike, located at the first scan point near the boundary of the beam, is likely due to end effect.

In the CDI plot for the second mode shape in Figure 4-23, the notch location correlates to a relatively large spike at the center. The notch is more evident in this mode shape because it is located at the maximum deflection. Additionally, there is a second large spike as well as a smaller spike. The second large spike is located at approximately 25% of the beam length and the smaller spike is located at approximately 80% of the beam length.

Upon visual inspection of the beam, the cause of these two additional spikes was discovered. At both locations, visible scarring was caused by clamping the beam in a vice to machine the support material and pins off the beam. The spike locations line up with where the end of the vice clamped the beams. During the machining operation, these locations would experience higher stress concentrations than the rest of the beam due to the milling operation and vibrations in the overhanging section of the beam.

Examining damages across the length of the beam reveals how critical the relationship between damage location and the deflection of the mode shapes is. For

example, the notch at the center of the beam is undetectable in the third mode shape in Figure 4-24 while it is the dominating feature in the second mode shape in Figure 4-23. This is because in Figure 4-23 the beam's maximum displacement is directly at the notch location while in Figure 4-24 the beam has little to no deflection at the notch location due to a node in the mode shape. Additionally, the relatively small irregularity located around 20% of the beam length is clearly visible as the largest feature in Figure 4-24, even though the notch is a much larger irregularity in the geometry of the beam. This means that when searching for damage using the CDI method, it is critical to investigate multiple mode shapes with nodes located at different points across the structure.

Table 4-4 lists details from each result of the CDI. The results for each beam vary, however there are patterns that are present throughout all beams. In all but three of the beams, damage can be clearly detected in the range of 40% to 60% of the beam length. In the cases where this damage was undetected, a large spike skewing the data may have overshadowed a possible spike at the center of the beam. Additionally, most of the beams experienced spikes toward the edges of the beam, related to the machining operation discussed above.

Table 4-4: Damage Detection from CDI Results

CDI Results	
Beam	Description (all percentages approximate)
N1	Damage detected at 20%, 45%, and 80% of beam length. Notch only detectable in Mode 2.
N2	Damage detected at 45% and 65% of beam length. No clear results in Mode 1.
N3	Damage detected at 30% and 82% of beam length. Spike at notch location overshadowed by surrounding spikes.
N4	Damage detected at 35% and 70% of beam length. Spike at notch location overshadowed by surrounding spikes.
N5	Damage detected at 30%, 50%, and 70% of beam length.
N6	Damage detected at 50% and 75% of beam length.
N7	Damage detected at 30%, 50%, and 80% of beam length. Mode 3 experiences high end effect interference.
N8	Damage detected at 20% and 50% of beam length. Mode 3 experiences large number of spikes.
N9	Damage detected at 30% and 65% of beam length. End effect amplitude overshadows results in Mode 2.
N10	Damage detected at 10%, 45%, and 85% of beam length. Mode 2 experiences high end effect spike.
N11	Damage detected at 35%, 60%, and 80% of beam length.
N12	Damage detected at 50% and 70% of beam length. End effect overshadows results of mode 3.
N13	Damage detected at 25%, 45%, and 85% of beam length. Large end effect in modes 1 and 2.
N14	Damage detected at 25%, 60%, and 90% of beam length.
N15	Large spike at 60% of beam length. Smaller spikes at 20% and 80% of beam length.
N16	Damage detected at 30%, 50%, and 80-90% of beam length. Many smaller spikes are observed.
N17	Damage detected at 20%, 40%, and 90% of beam length. Many smaller spikes are observed.
N18	Damage detected at 50% and 80% of beam length.
N19	Damage detected at 30%, 50%, and 80% of beam length.
N20	Damage detected at 10%, 60%, and 90% of beam length.

The final analysis tool used for damage detection is the continuous wavelet transform (CWT). The CWT is a tool that is used to detect discontinuities in signals.

Chapter 3 provides a detailed explanation about the usage of CWT for damage

detection. A graphical representation of the CWT for modes 1, 2, and 3 for beam N1 can be found in Figure 4-25, Figure 4-26, and Figure 4-27.

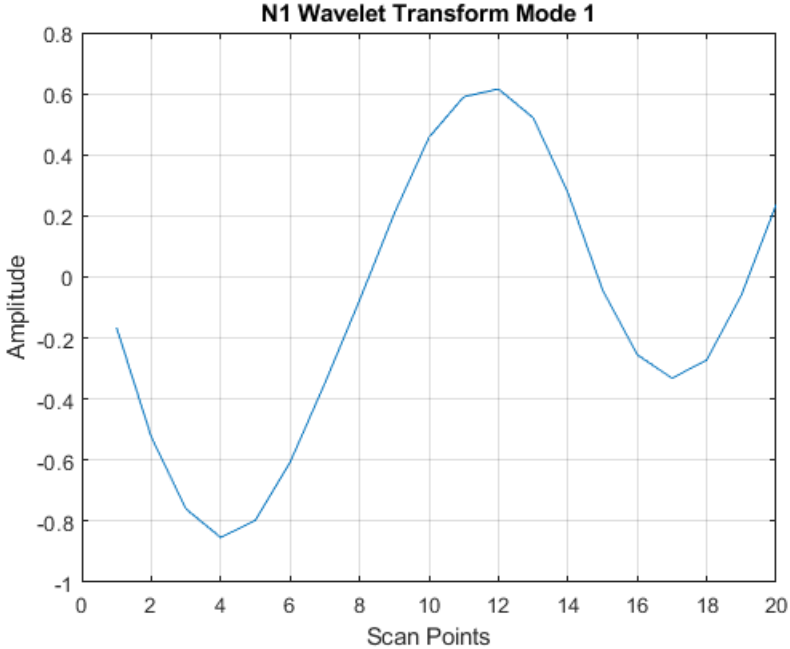


Figure 4-26: Beam N1 Mode 1 CWT

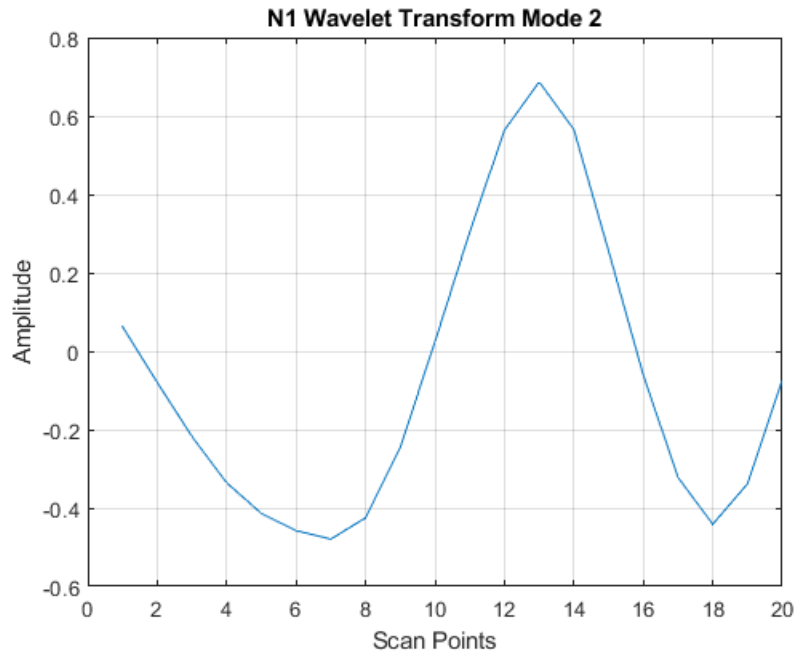


Figure 4-27: Beam N1 Mode 2 CWT

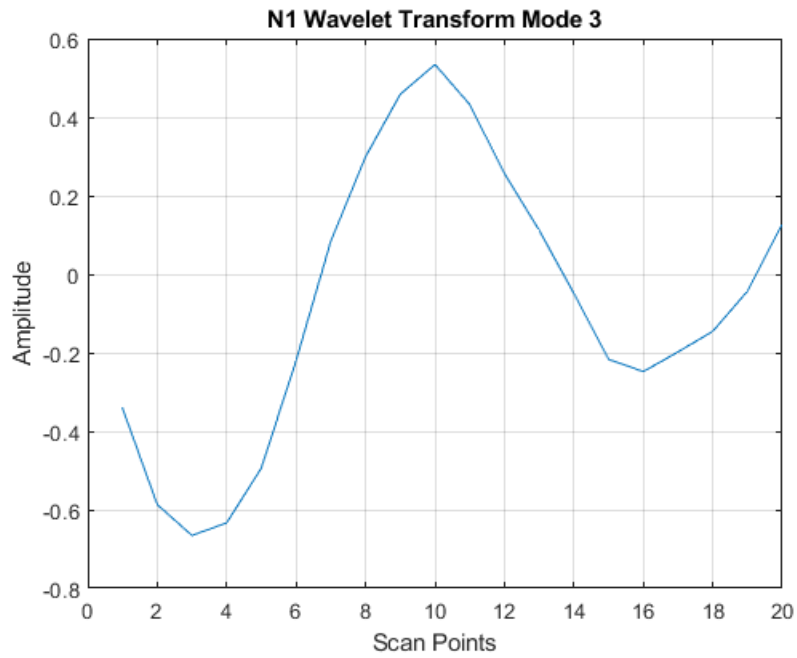


Figure 4-28: Beam N1 Mode 3 CWT

In Figure 4-25, Figure 4-26, and Figure 4-27, the x-axis relates to the scan points of the beam and the y-axis relates to the amplitude of the signal subject to the Wavelet transform. These graphs show the location as well as the size of any discontinuities detected. The higher the amplitude, the more significant the discontinuity can be expected to be. All three CWT graphs show three distinct discontinuities that correlate to the spikes in the CDI. However, the location of each discontinuity appears to change slightly for each mode shape. This suggests that the CWT is useful for detecting the presence and possibly the extent of damage in a structure, but the CWT may not necessarily be useful for detecting a specific damage location.

Table 4-5 lists the results for each beam after applying the wavelet transform. The results for most of the beams indicate three discontinuities along the length of the beam. This is consistent with the three spikes found in these beams from the CDI analysis. Some beams, such as beam N16, show more than three discontinuities. In these cases, these discontinuities could be due to end effects or the discontinuities could relate to actual anomalies in the beam. These anomalies could be caused by repeated re-fixturing in the CNC milling machine as the beams were removed for measuring.

Table 4-5: Damage Detection from Wavelet Results

Wavelet Results	
Beam	Description
N1	All mode shapes show three discontinuities.
N2	Mode 1 changes sign several times at center of beam. Modes 2 and 3 show three discontinuities.
N3	Mode 1 shows one discontinuity, mode 2 shows two discontinuities, mode 3 shows three discontinuities.
N4	All mode shapes show three discontinuities.
N5	Mode 1 unclear, modes 2 and 3 show three discontinuities.
N6	Mode 1 and 2 show three discontinuities, mode 3 shows four.
N7	All mode shapes show three discontinuities.
N8	Mode 1 shows 2 discontinuities, modes 2 and 3 show three.
N9	All mode shapes show three discontinuities.
N10	Modes 1 and 3 show three discontinuities, mode 2 shows two.
N11	All mode shapes show three discontinuities.
N12	All mode shapes show three discontinuities. Mode 2 shows two distinct peaks in the middle of the beam.
N13	All mode shapes show three discontinuities.
N14	Modes 1 and 3 show five discontinuities, mode 2 shows three.
N15	All mode shapes show three discontinuities.
N16	Modes 1 and 3 show five discontinuities, mode 2 shows four.
N17	Modes 1 and 3 show four discontinuities, mode 2 shows three.
N18	All mode shapes show three discontinuities.
N19	All mode shapes show three discontinuities.
N20	All mode shapes show three discontinuities.

4.2.3: Build Parameters and Damage Detection

A secondary goal of this study is to determine whether build parameters influence the detection of damage. Four different parameter sets have been used in this study and five notched beams were printed in each group. Five un-notched beams were printed using the default printing parameters. Table 4-6 lists the parameters used for each print.

Table 4-6: Beam Printing Parameters

Print Parameters		
Beam	Hatch Distance (mm)	Layer Thickness (mm)
U1 – U5	0.09	0.02
N1 – N5	0.09	0.02
N6 – N10	0.12	0.02
N11 – N15	0.09	0.04
N16 – N20	0.12	0.04

The CODS, CDI, and CWT analyses were performed for each of these beams. An example of the CDI for a beam in each of the altered parameter sets can be found in Figure 4-28, 4-29, and Figure 4-30. The results from these beams reiterate the results found for the default parameter sets. The notch located at the center of each beam is discernable as a spike approximately at the center of the graph. In the case of Figure 4-28 and Figure 4-30, there is possible interference from end effects towards the end of the beam. As seen in the case of beam N1, damage caused during the machining operation appears in the form of a spike at approximately 10 – 20% of the beam length and again at approximately 80% of the beam length. The CODS and CWT results for these parameter sets also closely match the results from the default parameter prints. The results for beams N10, N15, and N20 can be found in the Appendix.

Additionally, by analyzing Table 4-4 and Table 4-5, the results from each parameter set can be compared. As the parameters change, the same trends continue with the CDI as well as the CWT. Damage is located at approximately the center of each beam, and in many cases damage caused by the machining operation is also found. Since the results vary similarly across all parameter sets, no conclusions can be drawn about how these parameters affect the detection of damage.

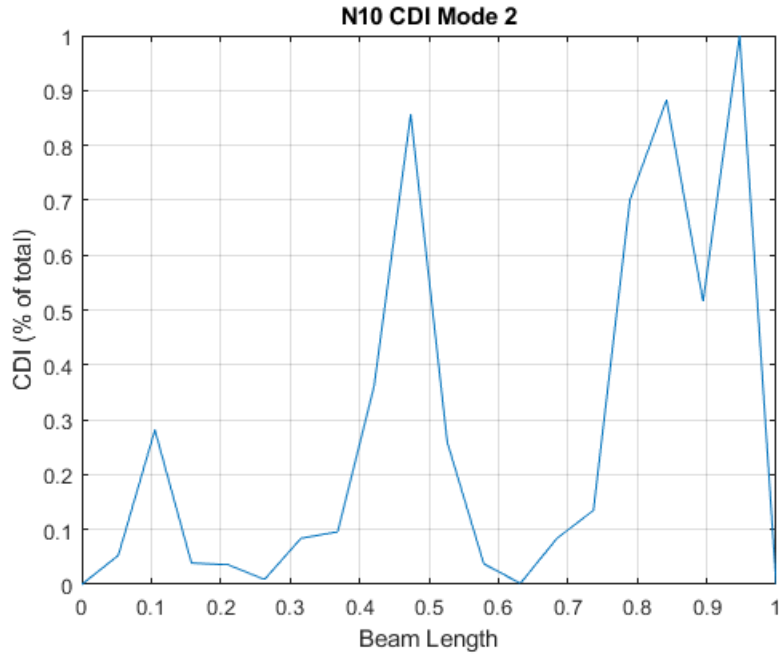


Figure 4-29: Beam N10 Mode 2 CDI

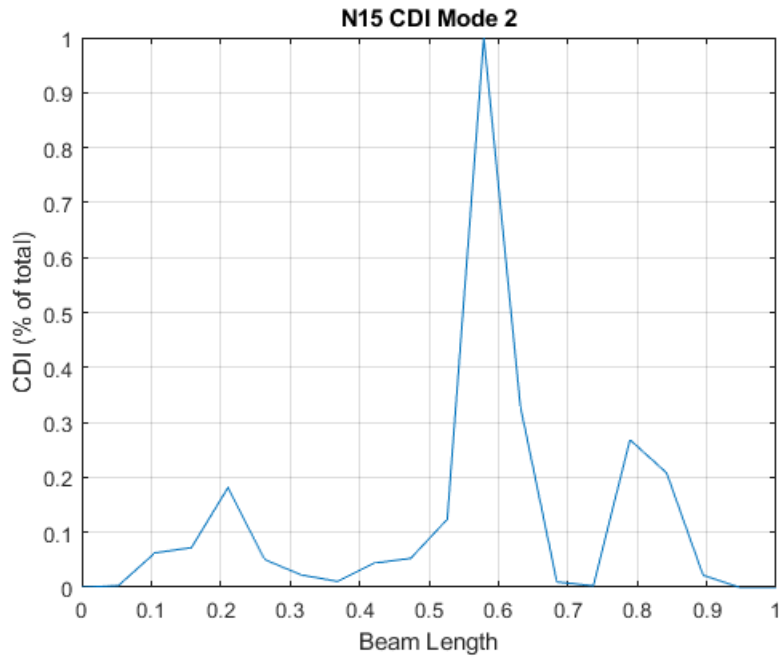


Figure 4-30: Beam N15 Mode 2 CDI

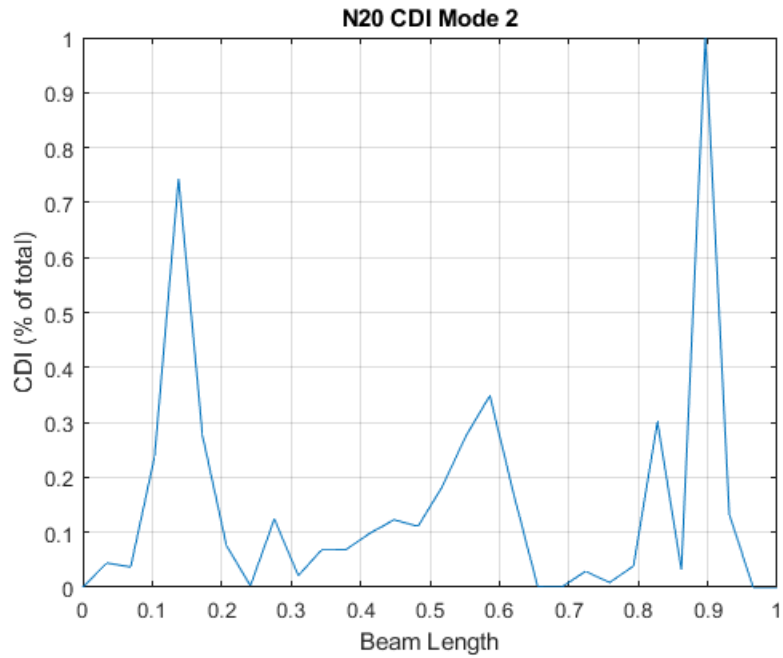


Figure 4-31: Beam N20 Mode 2 CDI

4.3: Conclusions

As seen in the findings in this chapter, the results generated for beam N1 have been successful in detecting damage in the beam. This includes the damage introduced in the form of a notch as well as unexpected damage that was caused during finishing operations of the beam. Examining multiple mode shapes reveals how damage can be clearly visible at one frequency and nearly invisible at another. This demonstrates that for damage detection multiple mode shapes of a part must be examined to ensure that the entire geometry of the part is checked for damage.

For each parameter set tested in this study, the central notch and damage caused during the machining operation have been similarly located. Altering the layer thickness and the hatch distance of the print did not appear to impact the way these tests detect and locate damage. These similarities extend to the measured displacements, the CODS, the CDI, and the CWT.

The different analysis tools used in this study have proved to be useful for detecting damage for different reasons. The CWT is useful because it clearly shows the presence of three distinct discontinuities in the mode shapes. The drawback appears to be that the exact location of the damage is difficult to determine with the CWT. Meanwhile, the CDI has been useful in pinpointing the location of damage. The CDI appears to correctly identify a previously unknown damage location that was visually verified. The drawback of the CDI is that it can be difficult to differentiate between spikes due to damage and spikes due to end effects or noise. To more accurately and confidently detect damage, a combination of CDI and CWT analysis may need to be performed across multiple natural frequencies and mode shapes.

CHAPTER FIVE: CONCLUSIONS AND FUTURE SCOPE

Since direct metal laser sintering (DMLS) is a relatively new additive manufacturing process, there is a need to understand the kinds of damage that cause failure in parts manufactured by this process. This study investigates possible means of damage diagnostics in such parts by using laser vibrometry. This chapter provides a summary of the results and some of the main findings from this research.

5.1: Summary:

This study set out to determine if using a laser vibrometer is viable to detect damage in 316L stainless steel DMLS parts. This is particularly important because laser vibrometry is a non-destructive technique as well as a non-contact process. Additionally, the role of DMLS process parameters and their influence on the way damage is manifested in DMLS parts has also been investigated. An EOS M290 DMLS machine has been used to print the parts and a PSV-400 scanning laser vibrometer has been used to analyze the parts.

Beams have been used as the specimen for this study. To print the beams, the geometry was modeled in Creo Parametric 3.0 and post processed using a combination of Materialize Magics (version 22.0) to prepare the .stl file and EOS Print (version 2.0) to layout the build plate. Support material was machined off the beams using a HAAS vf3 mill. EOS Print was also used to control the print parameters for each beam. The variable parameters chosen for this study were the layer thickness and the hatch distance due to their critical influence on build time.

To test the beams, a fixture was used to hold the beams and attach the vibration generator and scanned by the PSV-400. The beams were tested in a range from 0 Hz to 10Khz with a resolution of 3.125 Hz. Generally, 20 scan points were created in a single line through the center of each beam. Some beams were tested again with 30 scan points; however, this increase in scan time did not meaningfully change the results. The natural frequencies were then identified and mode shapes were used to compare the damaged and undamaged parts.

5.2: Conclusions:

Overall, this study has been successful in detecting damage in beams manufactured from the DMLS process. This includes detecting a notch that has been designed into the geometry of the beams as well as detecting other anomalies that were caused by stresses generated during machining operations to post-process the parts. The stress concentration at the notch was further accentuated by generating a small crack at the end of the notch. The first three bending mode shapes of each beam have been used for evaluating damage by comparing these modes to an undamaged beam.

Damage has been successfully detected by using the curvature damage index (CDI). CDI clearly captures damage in the form of a spike while plotting this index across the length of the beam. It is necessary to analyze several bending modes with nodes at varying positions across the length of the beam. Due to low beam deflections at node positions, damage located close to a node is difficult to detect, therefore requiring multiple modes. Analyzing multiple mode shapes overcomes the difficulty posed by node locations.

The CDI has been useful in detecting the notch in all but two of the beams, N3 and N4. In these beams, spikes located at the center of the beam were overshadowed by spikes at other locations. This could be attributed to end effects and noise in the scan results. In all beams, the most reliable mode to detect the notch location was found to be the second mode. This is primarily because there is no node located at or near the notch location in this mode.

The continuous wavelet transform (CWT) has also been useful in detecting damage in the beams tested for this study. The CWT is successful in reporting discontinuities in the beams correlating to the damage location. The CWT has been used for all three bending mode shapes. While the node locations seem to have a major effect on damage detection through the CDI technique, nodes do not play a major role in damage detection by the CWT. However, CWT does not provide a clear location of damage, as compared to the CDI.

In addition to detecting the damage that was created in the test parts, the laser vibrometer scans successfully detected and located additional anomalies that were previously unknown. Spikes in the CDI results correlated with scarring caused during machining operations that were performed to post-process the parts. These scars relate to stress concentrations that are indicative of damage.

In all but three beams, N2, N6, and N18, both anomalies have been successfully detected. In the case of these three beams, one of the two anomalies was detected. Mode 3 was the most useful mode to detect these anomalies due to the lack of a node at or near the damage location. These spikes were visible in mode 1, however due to

end effects it was more difficult to determine whether these spikes in this mode were due to noise or damage.

In all beams, the CWT detected an anomaly approximately at the center of the beam and at least two more near the anomalies detected in the CDI. Several CWT results indicated damage clustered near these anomalies. This could be due to fixturing, removing, and re-fixturing the beams in the vf3 mill to take measurements during the milling operation. Re-fixturing could slightly move the location of stress concentrations, causing additional anomalies to be found in the tests.

The results of this study found that detection and location of damage by using vibrational mode shapes is feasible by using both the methods, CDI as well as CWT, that were investigated in this study. The CDI is useful for detecting locations of damage while the CWT is useful in detecting the number of discontinuities present. Additionally, it is found that it is necessary to test at several mode shapes to ensure that nodes in the mode shapes do not mask any damage as well as to reduce the likelihood of end effects and noise interferences that are common at relatively lower frequencies. Results indicate that it may be important to use both methods in conjunction to mitigate the possibility of missing damage detection due to noise or end effects or node locations.

Comparing results of parts made from different process parameters does not reveal any obvious patterns for damage diagnostics. This suggests that changing the DMLS process parameters does not have any direct effect on the kind of damage investigated during this research. This may need to be investigated further by looking at different modes of damage on different parts or by investigating other process parameters of the DMLS process.

The research questions that this study sought to answer are as follows:

- 1) Can damage of DMLS parts be detected from the mode shapes measured with a laser vibrometer?
- 2) Can these mode shapes be used to predict or locate damage in parts?
- 3) Do mode shapes of damaged parts differ with process parameters associated with the SLM process?

From the results of the CDI and CWT analysis, these questions can be answered. It can be concluded that damage of DMLS parts can be detected by directly comparing mode shapes of a damaged part to an undamaged part. The damage is clearly detected in the form of a spike in the CDI and as a discontinuity in the CWT. The CWT is particularly useful in detecting the quantity of potential damage sites in a part by noting changes in the slope sign. A change in the slope sign indicates the presence of an anomaly.

The mode shapes in this study have also been successful in predicting and locating damage in parts. The CDI results were used to locate previously unknown anomalies in each beam. The locations of unexpected spikes on the CDI plots were traced back to the corresponding location of the beams. At these locations, anomalies caused during post-process machining operations were observed. These anomalies were unknown prior to the CDI analysis.

Comparing results between beams manufactured with different process parameters did not reveal any discernable pattern related to layer thickness or hatch distance. This can be concluded for the CDI as well as the CWT analysis. However, it

may be noted that only two process parameters have been investigated in this study. Therefore, the influence of process parameters will need to be investigated further.

5.3: Future Scope:

This study investigated simple cantilever beams by using a specific scan setup in the PSV-400 laser vibrometer. In the future, this project could be expanded by including complex structures with scan points in 2D or 3D. Additionally, the capability of the laser vibrometer can be further investigated to create better scan results for complex parts with varying damage locations. The laser vibrometer is a particularly useful tool for this task because it is a non-contact test method. This means that the PSV-400, unlike other tools such as a strain gage, does not influence the behavior of the part due to contact. Additionally, the location of the test can be easily and quickly changed to test multiple locations in a single test. Furthermore, a part can be tested in a non-destructive manner and while it is functional.

With regard to the laser vibrometer, there are several steps that could be taken to improve the quality of results. Currently, the vibration generator and the scanning head are mounted on the same table. Ideally, the scanning head should be isolated from the vibrations generated during testing. This could be accomplished by mounting the scanning head on a separate tripod. This may be particularly important if the amplitude of excitations is significant.

The structures that are used for damage detection can be significantly expanded in future studies. For instance, a complex truss structure or a frame with multiple parts could be used with different locations of damage at critical points. This will allow an investigation of the robustness of the damage detection techniques that have been

investigated in this study. Comprehending how damage is detected by analyzing mode shapes through the use of the wavelet transform or the curvature damage index would be a critical step in determining the usefulness of these methods for large, complex and real-life structures.

Additionally, more types of damage could be simulated instead of a notch that was investigated for this research. This could include cyclic fatigue testing parts to failure at locations of high stress concentration. Investigating damage of assemblies fastened together or parts that are welded together with a need to withstand complex loading conditions would test the viability of the damage diagnostics methods studied in this research.

REFERENCES

- [1] K. Roy and A. Ray-Chaudhuri, "Fundamental mode shape and its derivatives in structural damage localization," *Journal of Sound and Vibration*, vol. 332, no. 21, pp. 5584-5593, 14 October 2013.
- [2] S. Bremen, W. Meiners and A. Diatlov, "Selective Laser Melting A manufacturing technology for the future?," *Laser Technik Journal*, vol. 9, no. 2, pp. 33-38, April 2012.
- [3] ASTM, "Standard Terminology for Additive Manufacturing," *Standard F2792-12a*, 2015.
- [4] Y. Tang and Y. F. Zhao, "A survey of the design methods for additive manufacturing to improve functional performance," *Rapid Prototyping Journal*, pp. 569-590, 2016.
- [5] D. Bourell, M. Leu and D. Rosen, "Roadmap for Additive Manufacturing: Identifying the Future of Freeform Processing," The University of Texas, Austin, TX, 2009.
- [6] S. Abhishek Kumar and C. Sriram, "Technique to Enhance FDM 3D Metal Printing," *Bonfring International Journal of Industrial Engineering and Management Science*, pp. 128-134, 2016.
- [7] A. Angrish, "A critical analysis of additive manufacturing technologies for aerospace applications," in *IEEE Aerospace Conference*, Big Sky, MT, 2014.
- [8] J. Lopez-Castro, A. Marchal, L. Gonzalez and J. Botana, "Topological optimization and manufacturing by Direct Metal Laser Sintering of an aeronautical part in 15-5 Stainless steel," *Procedia Manufacturing*, pp. 818-824, 2017.
- [9] R. Domrose and T. Grunberger, "Identification of process phenomena in DMLS by optical in-process monitoring," *Laser Technik Journal*, pp. 45-48, 2015.
- [10] S. Rothberg, M. Allen, P. Castellini, D. Di Maio, J. Dirckx, D. Ewins, B. Halkon, P. Muyshondt, N. Paone, T. Ryan, H. Steger, E. Tomasini, S. Vanlanduit and J. Vignola, "An international review of laser Doppler vibrometry: making light work of vibration measurement," *Optics and Lasers in Engineering*, pp. 11-22, 2016.
- [11] J.-T. Kim, Y.-S. Ryu, H.-M. Cho and N. Stubbs, "Damage identification in beam-type structures: frequency-based method vs mode-shape-based method," *Engineering Structures*, pp. 57-67, 2003.
- [12] R. G. Budynas and J. K. Nisbett, *Mechanical Engineering Design*, New York: McGraw-Hill, 2011.
- [13] M. Norton and D. Karczub, *Fundamentals of Noise and Vibration Analysis for Engineers*, Cambridge: The Press Syndicate of the University of Cambridge, 2003.
- [14] D. Dessi and G. Camerlengo, "Damage Identification Techniques via Modal Curvature Analysis: Overview and Comparison," *Mechanical Systems and Signal Processing*, pp. 52-53, 2014.

- [15] "About ANSYS," 12 March 2018. [Online]. Available: <https://www.ansys.com/about-ansys>.
- [16] P. Thejasree, G. Dileep Kumar and S. Leela Prasanna Laksmi, "Modeling and Analysis of Crankshaft for passenger car using ANSYS," in *AMMMT*, 2016.
- [17] "Finite," 12 March 2016. [Online]. Available: <https://www.merriam-webster.com/dictionary/finite>.
- [18] Y. Wen, X. Yue, J. H. Hunt and J. Shi, "Feasibility analysis of composite fuselage shape control via finite element analysis," *Journal of Manufacturing Systems*, pp. 272-281, 2018.
- [19] D. L. Logan, *A First Course in the Finite Element Method*, Cengage Learning, 2--12.
- [20] S. Rao, *Mechanical Vibration*, Pearson.
- [21] S. W. Bostic, *Lanczos Eigensolution Method for High-Performance Computers*, 1991.
- [22] H. Gu, H. Gong, D. Pal and B. Stucker, "Influence of Energy Density on Porosity and Microstructure of Selective Laser Melted 17-4PH Stainless Steel," in *24th Annual International Solid Freeform Fabrication Symposium*, 2013.
- [23] D.-M. Chen, Y. F. Xu and W. D. Zhu, "Damage Identification of Beams Using a Continuously Scanning Laser Doppler Vibrometer System," *Journal of Vibration and Acoustics*, pp. 1-16, 2016.
- [24] J.-M. Yang, Z.-W. Yang and C.-M. Tseng, "Damage Detection in Stiffened Plates by Wavelet Transform," *International Journal of Naval Architecture and Ocean Engineering*, pp. 126-135, 2011.
- [25] M. Rucka and K. Wilde, "Application of Continuous Wavelet Transform in Vibration Based Damage Detection Method for Beams and Plates," *Journal of Sound and Vibration*, pp. 536-550, 2006.
- [26] S. Kaul, "Crack Diagnostics in Beams using Wavelets, Kurtosis and Skewness," *Nondestructive Testing and Evaluation*, pp. 99-112, 2013.
- [27] S. Yang and M. S. Allen, "Output-Only Modal Analysis Using Continuous-Scan Laser Doppler Vibrometry and Application to a 20kW Wind Turbine," in *IMAC, A Conference on Structural Dynamics*, 2011.
- [28] J. L. Semmlow and B. Griffel, *Biosignal and Medical Image Processing*, CRC Press, 2014.

APPENDIX A: EXAMPLE BEAM RESULTS

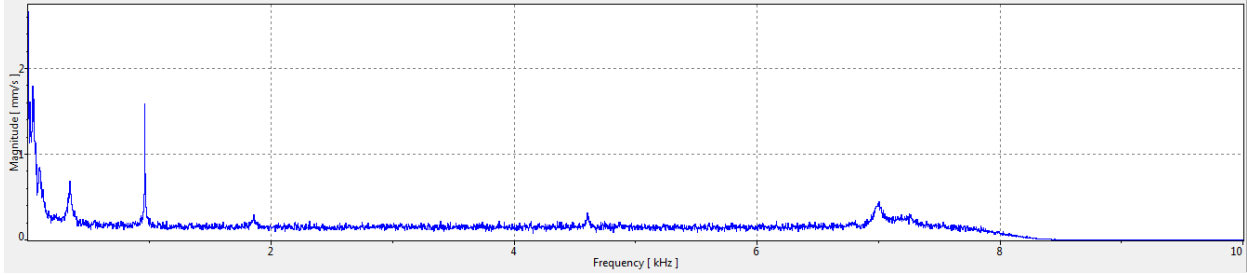


Figure A-1: Beam U1 Frequency Response

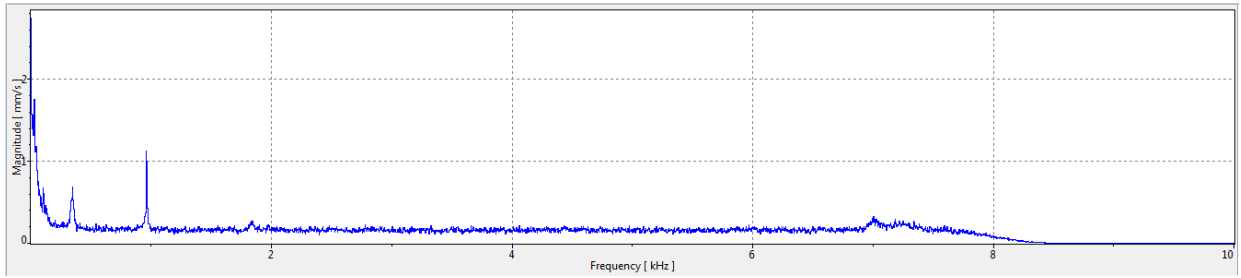


Figure A-2: Beam N1 Frequency Response

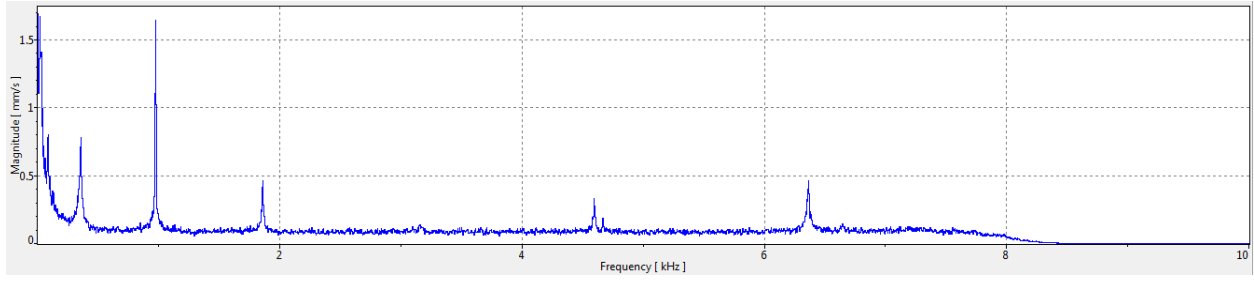


Figure A-3: Beam N10 Frequency Response

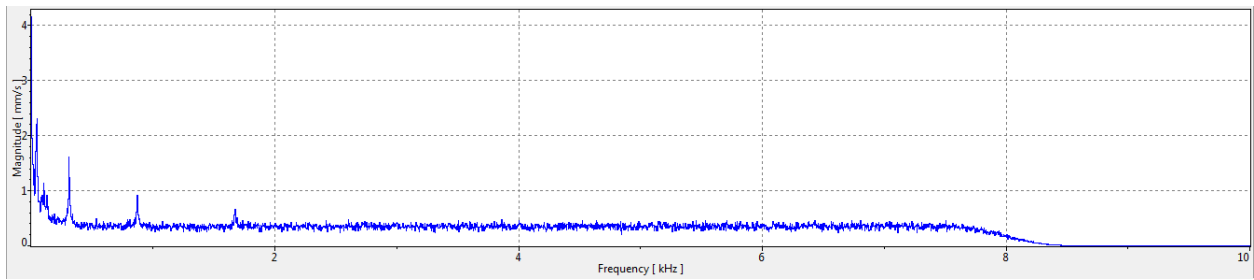


Figure A-4: Beam N15 Frequency Response

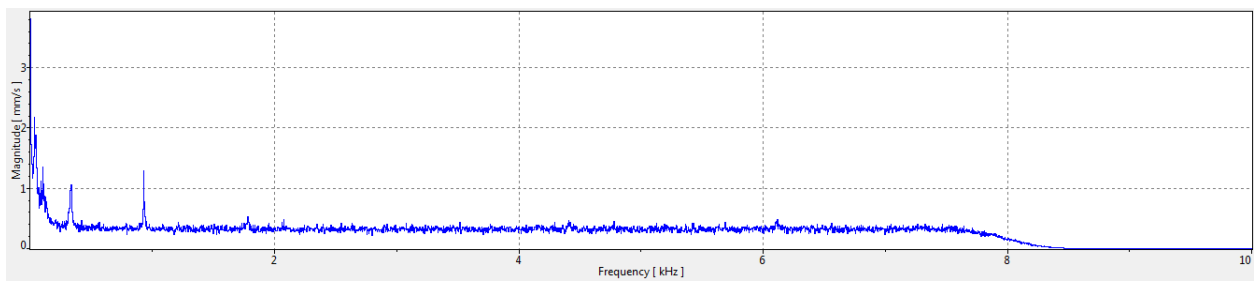


Figure A-5: Beam N20 Frequency Response

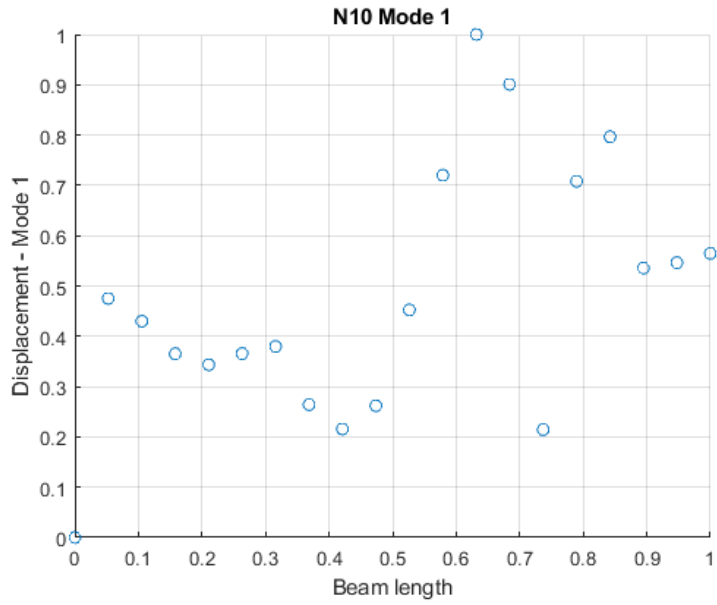


Figure A-6: Beam N10 Mode 1 Displacement

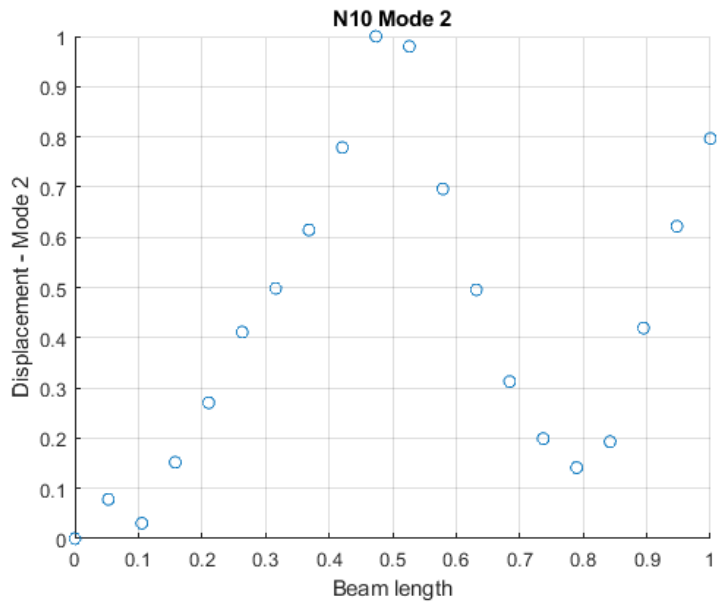


Figure A-7: Beam N10 Mode 2 Displacement

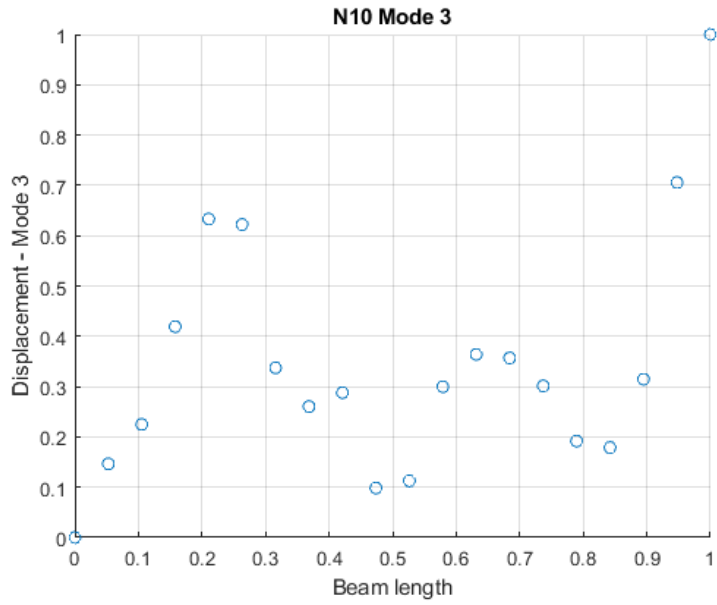


Figure A-8: Beam N10 Mode 3 Displacement

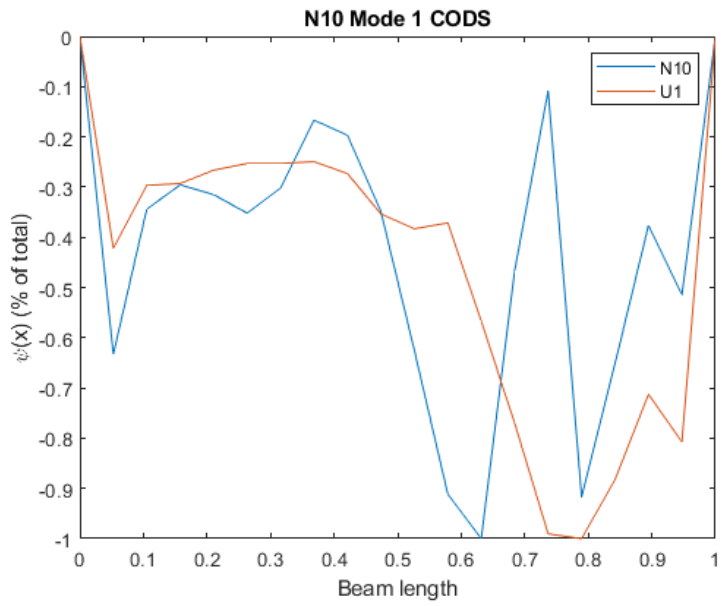


Figure A-9: Beam N10 Mode 1 CODS

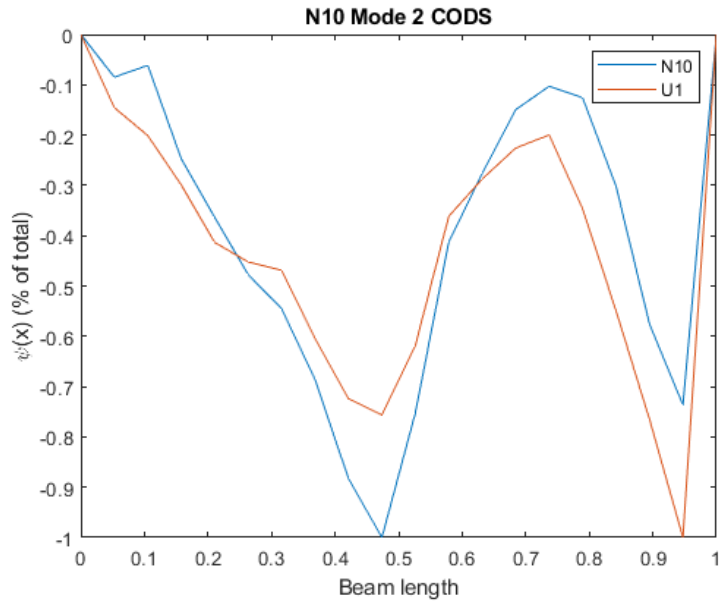


Figure A-10: Beam N10 Mode 2 CODS

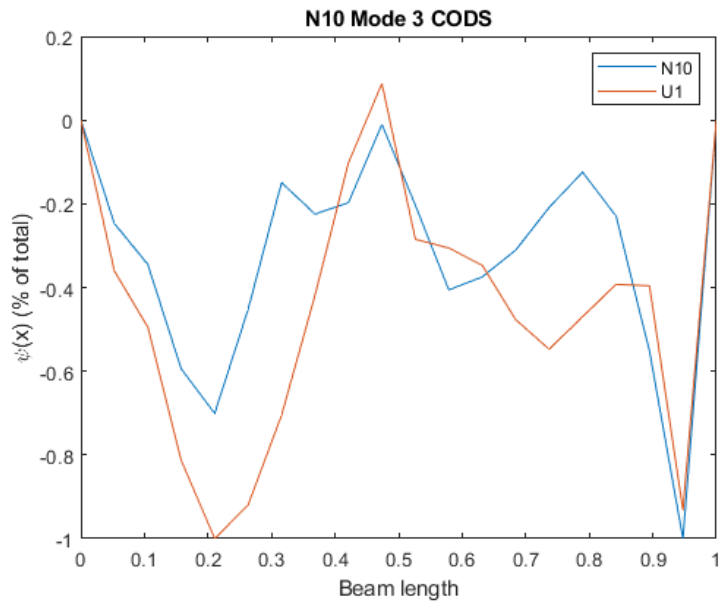


Figure A-11: Beam N10 Mode 3 CODS

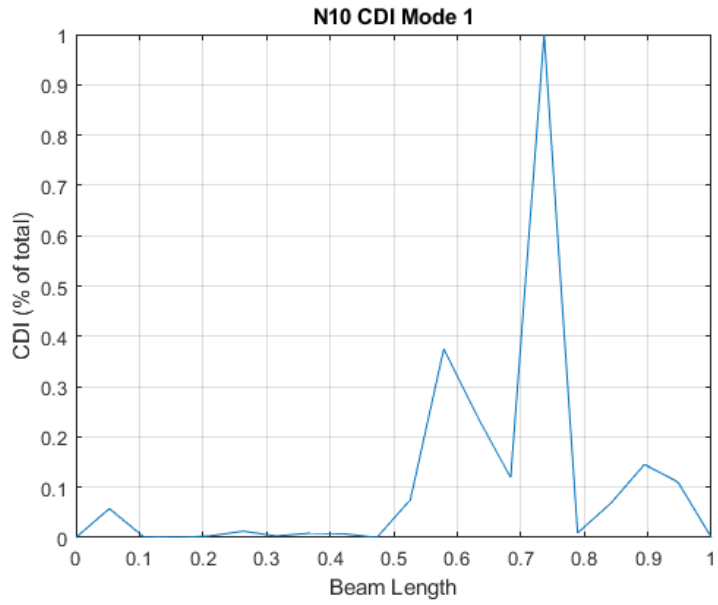


Figure A-12: Beam N10 Mode 1 CDI

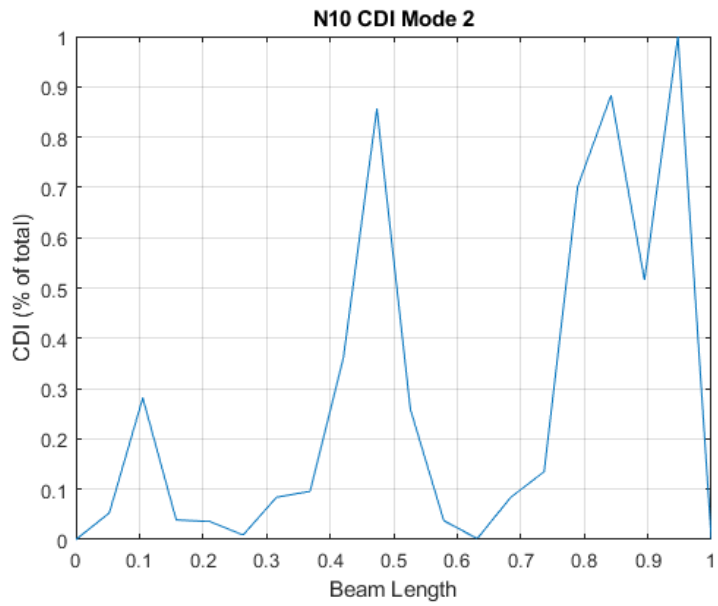


Figure A-13: Beam N10 Mode 2 CDI

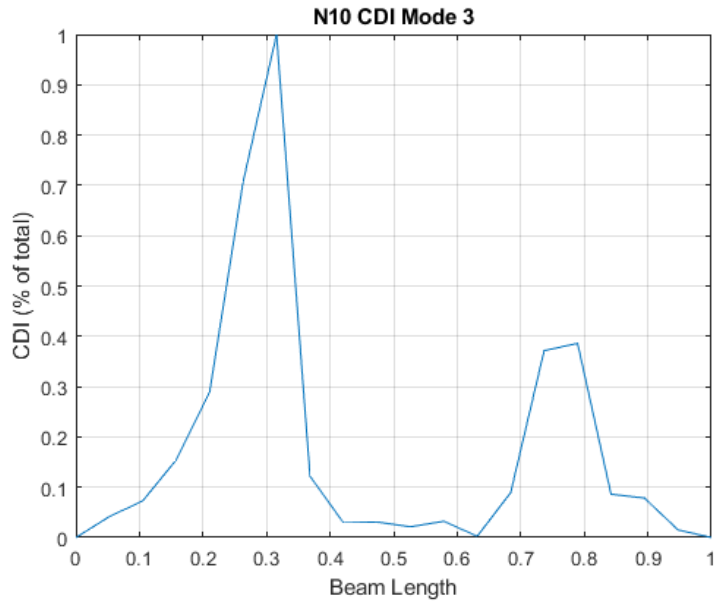


Figure A-14: Beam N10 Mode 3 CDI

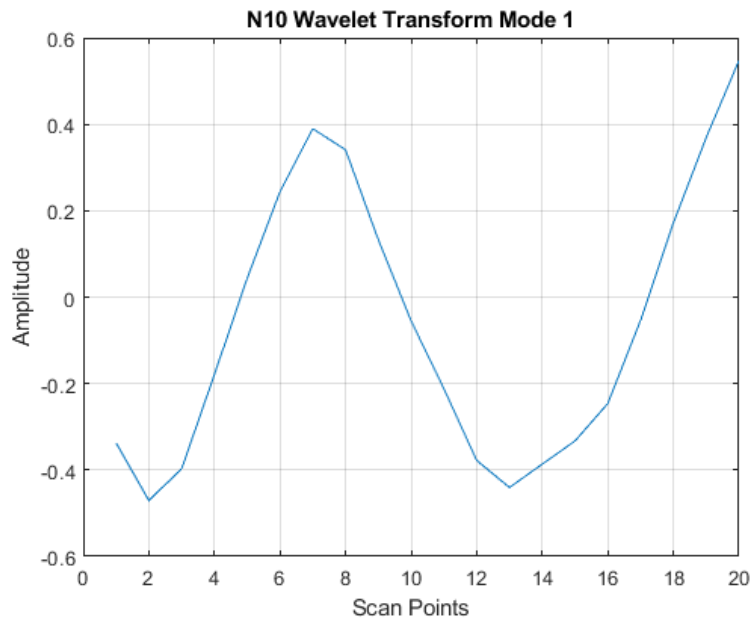


Figure A-15: Beam N10 Mode 1 CWT

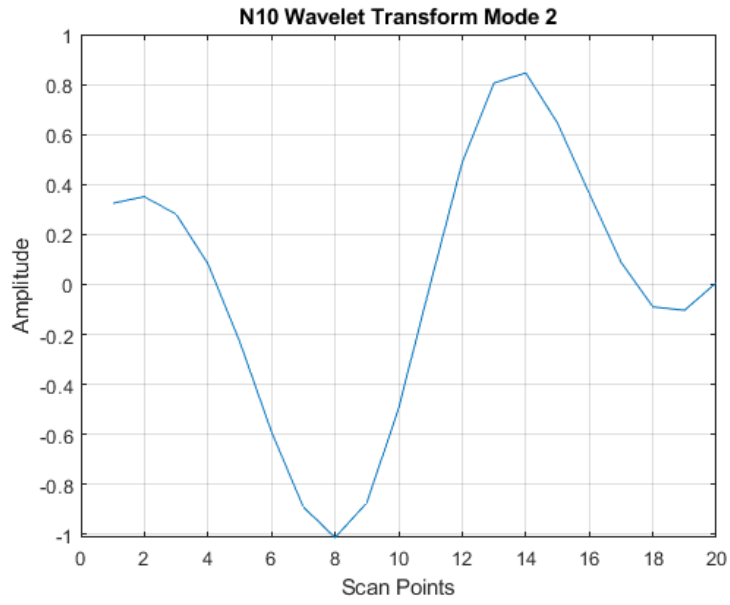


Figure A-16: Beam N10 Mode 2 CWT

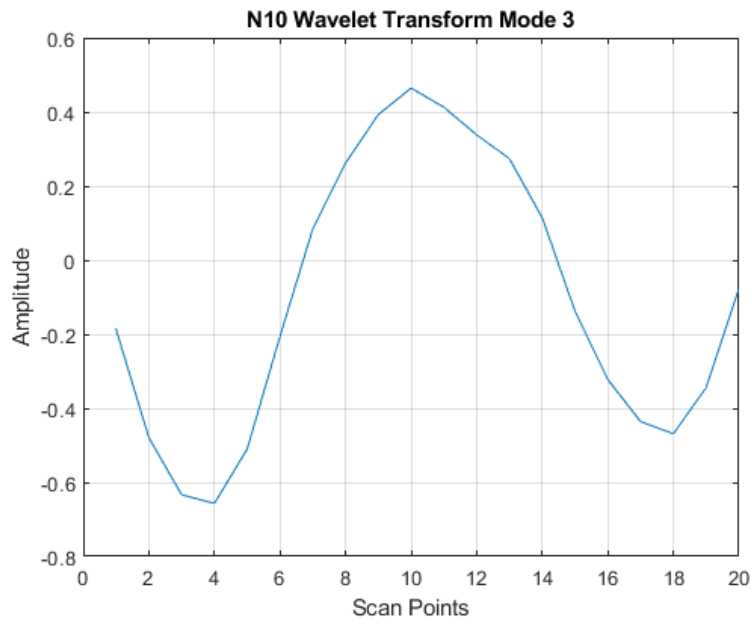


Figure A-17: Beam N10 Mode 3 CWT

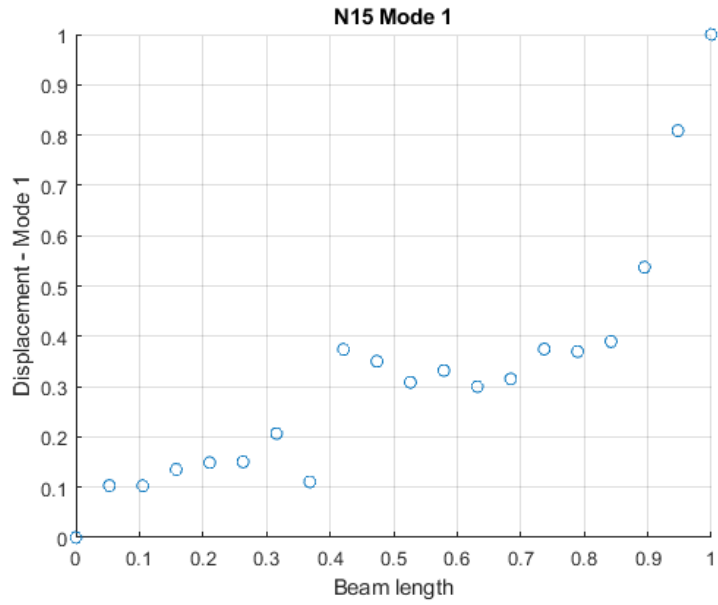


Figure A-18: Beam N15 Mode 1 Displacement

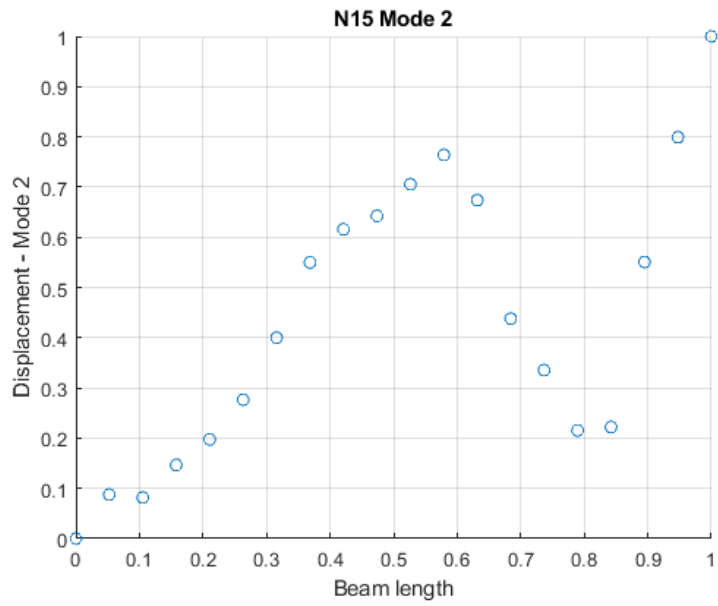


Figure A-19: Beam N15 Mode 2 Displacement

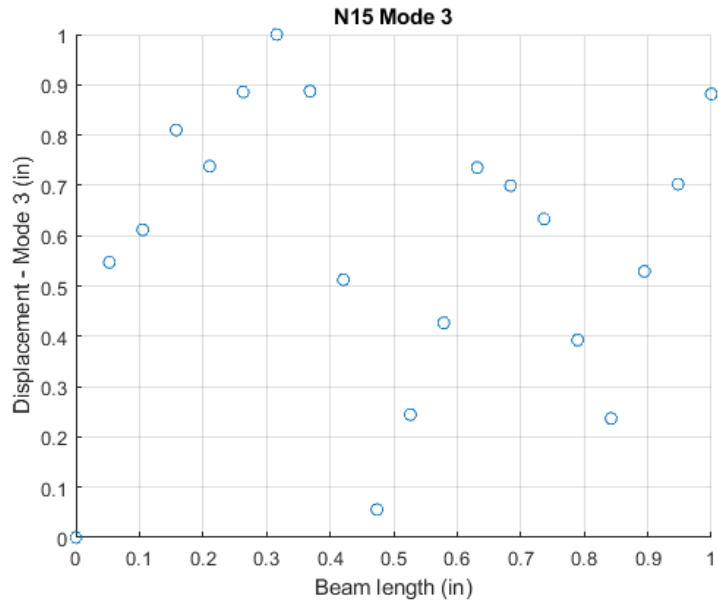


Figure A-20: Beam N15 Mode 3 Displacement

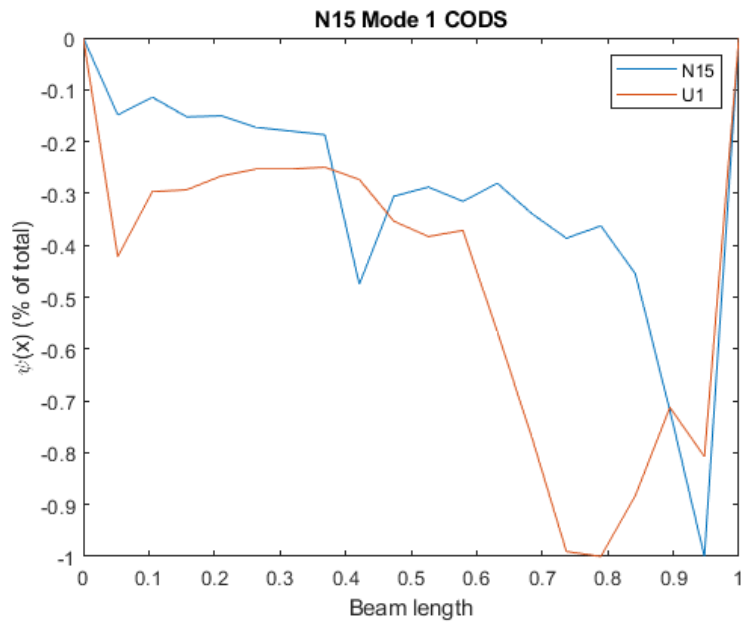


Figure A-21: Beam N15 Mode 1 CODS

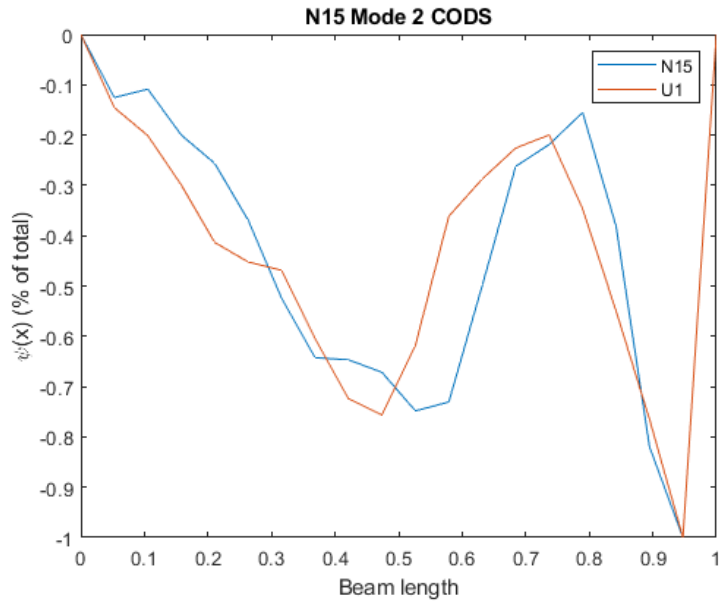


Figure A-22: Beam N15 Mode 2 CODS

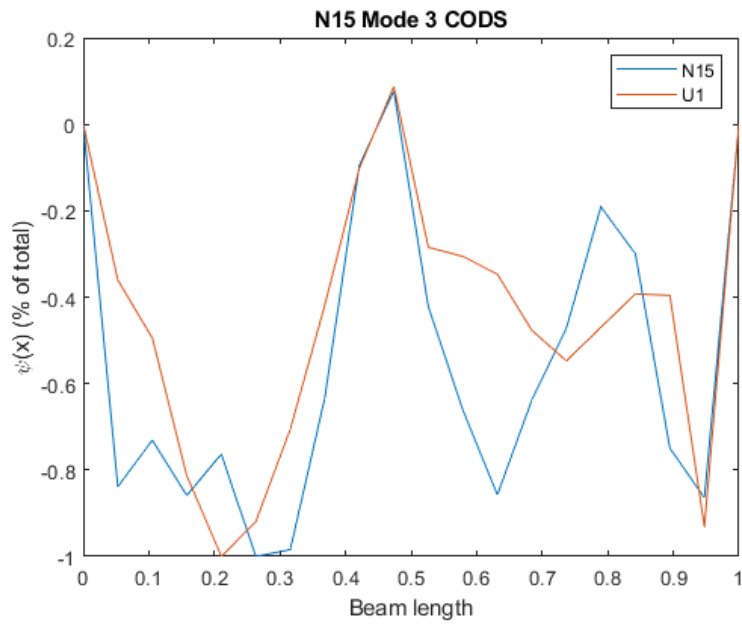


Figure A-23: Beam N15 Mode 3 CODS

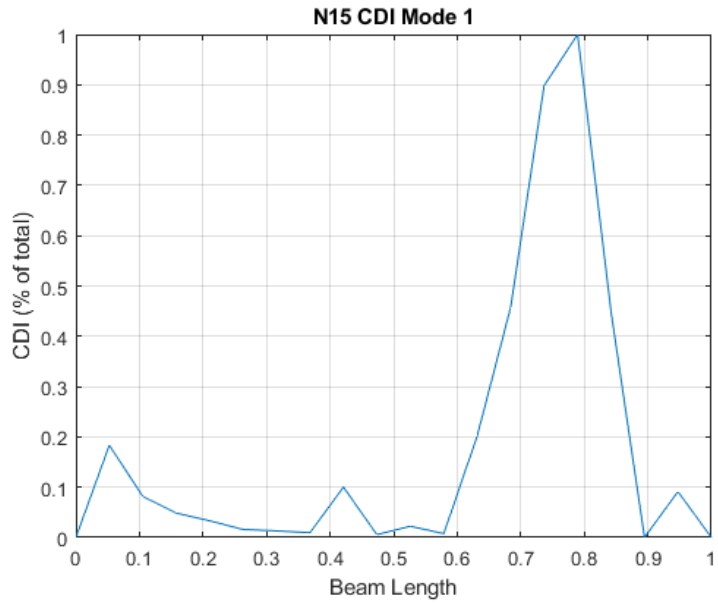


Figure A-24: Beam N15 Mode 1 CDI

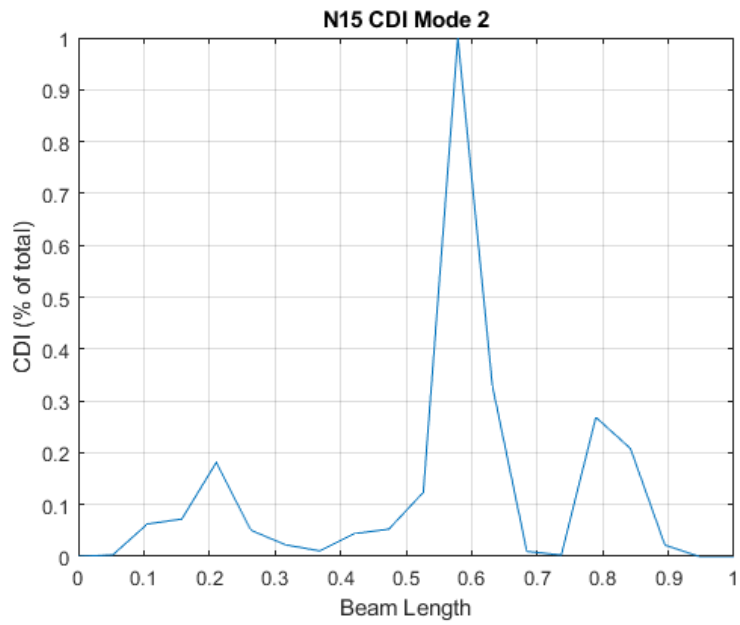


Figure A-25: Beam N15 Mode 2 CD

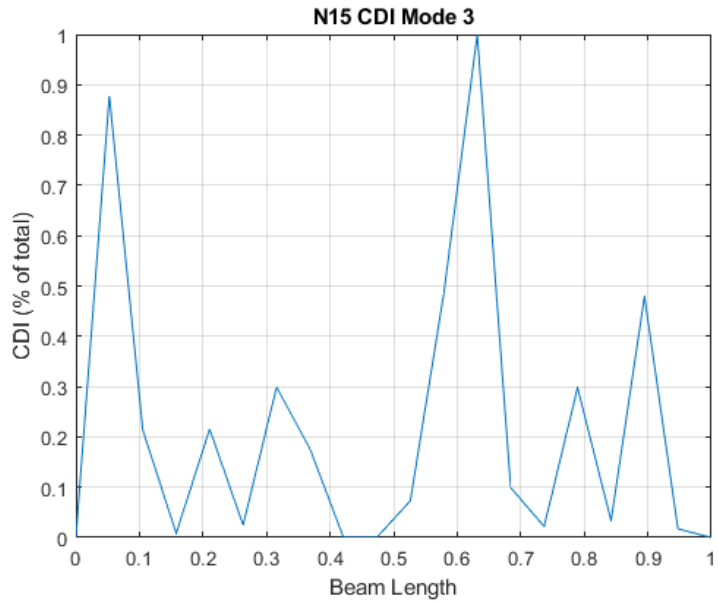


Figure A-26: Beam N15 Mode 3 CDI

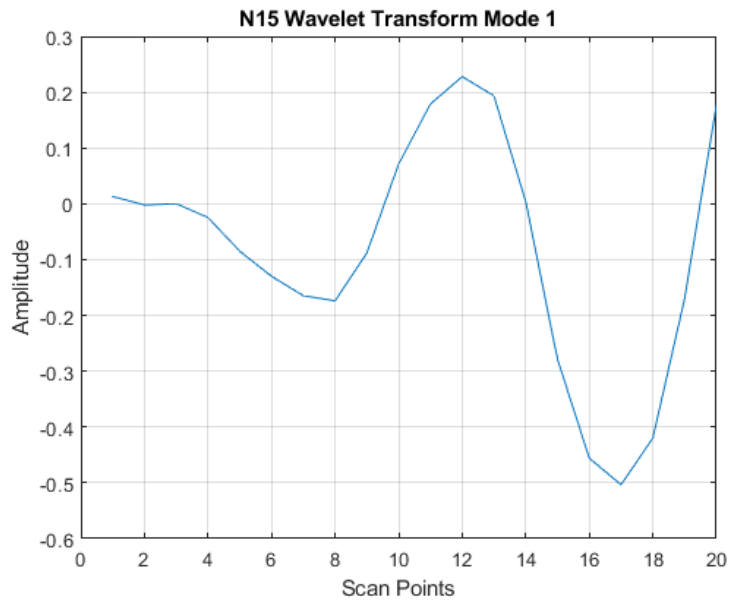


Figure A-27: Beam N15 Mode 1 CWT

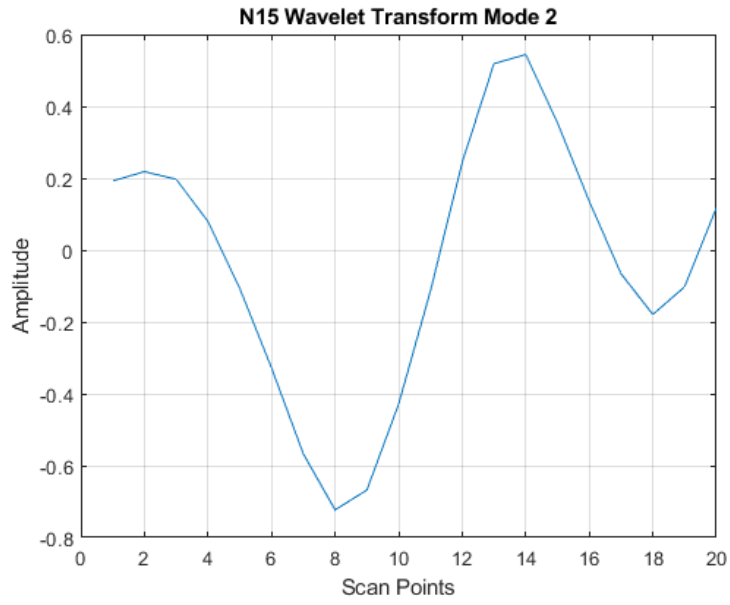


Figure A-28: Beam N15 Mode 2 CWT

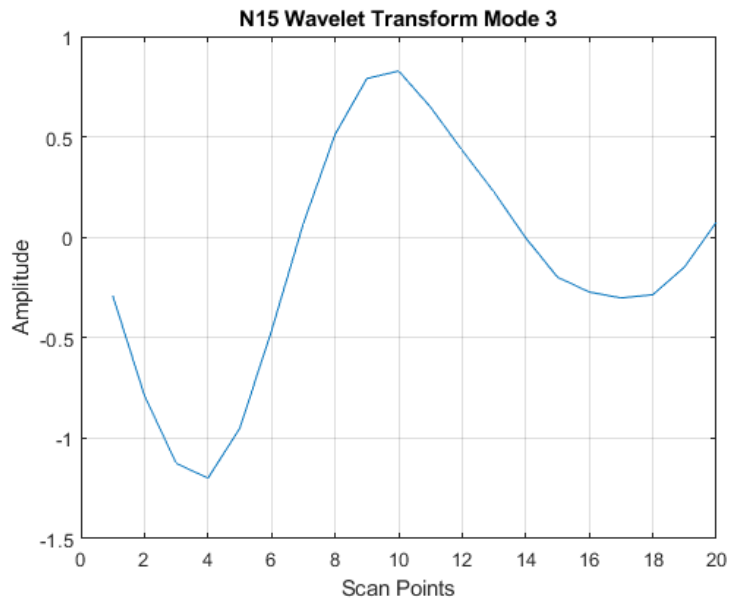


Figure A-29: Beam N15 Mode 3 CWT

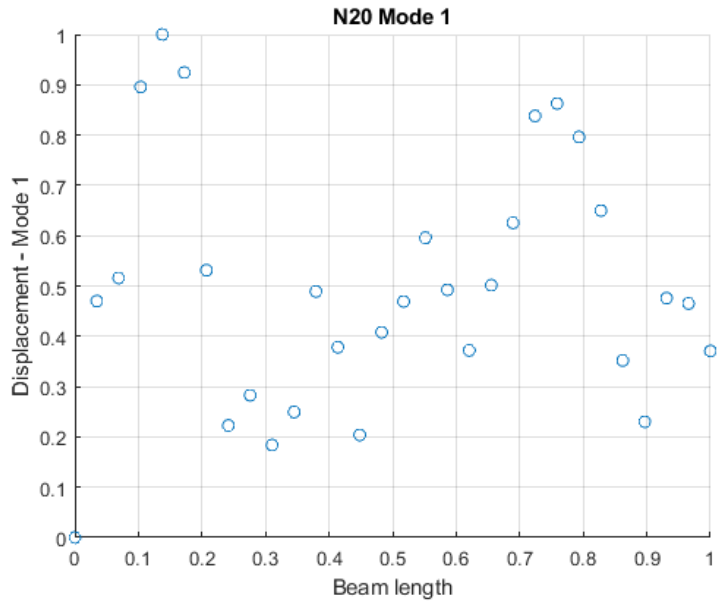


Figure A-30: Beam N20 Mode 1 Displacement

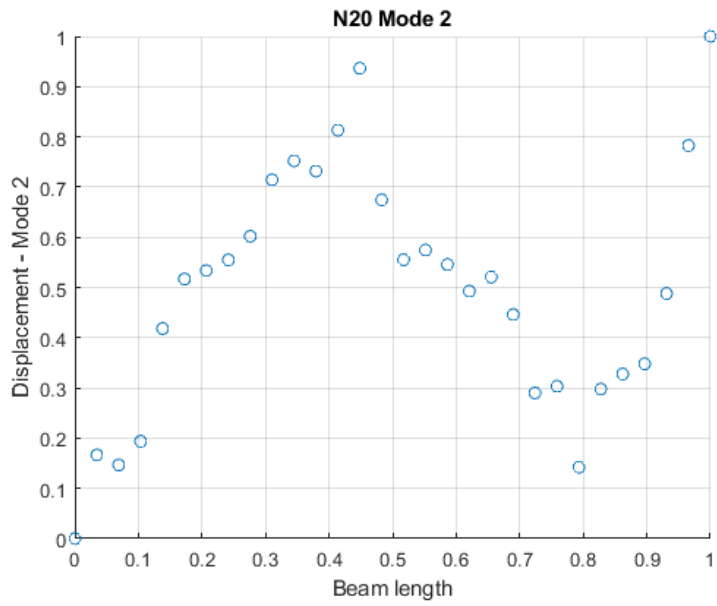


Figure A-31: Beam N20 Mode 2 Displacement

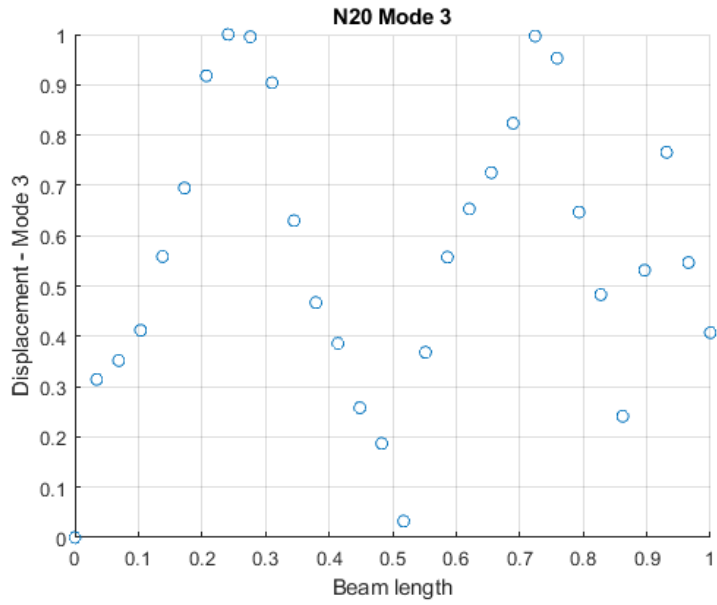


Figure A-32: Beam N20 Mode 3 Displacement

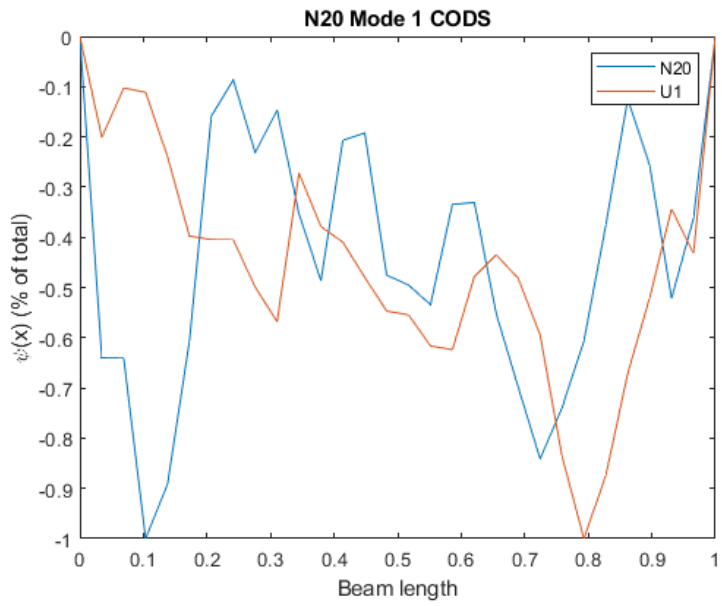


Figure A-33: Beam N20 Mode 1 CODS

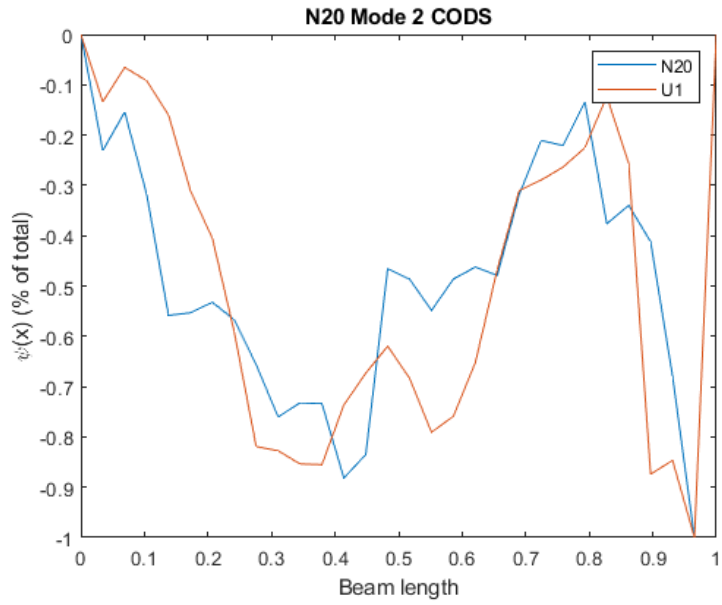


Figure A-34: Beam N20 Mode 2 CODS

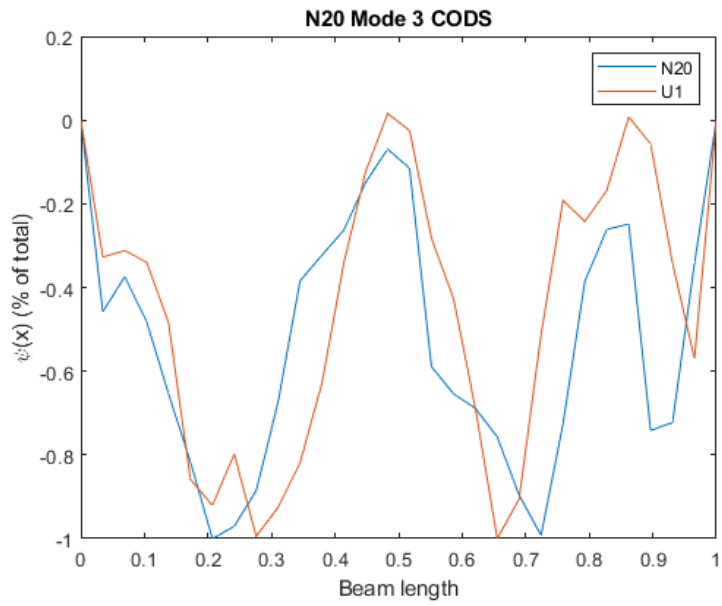


Figure A-35: Beam N20 Mode 3 CODS

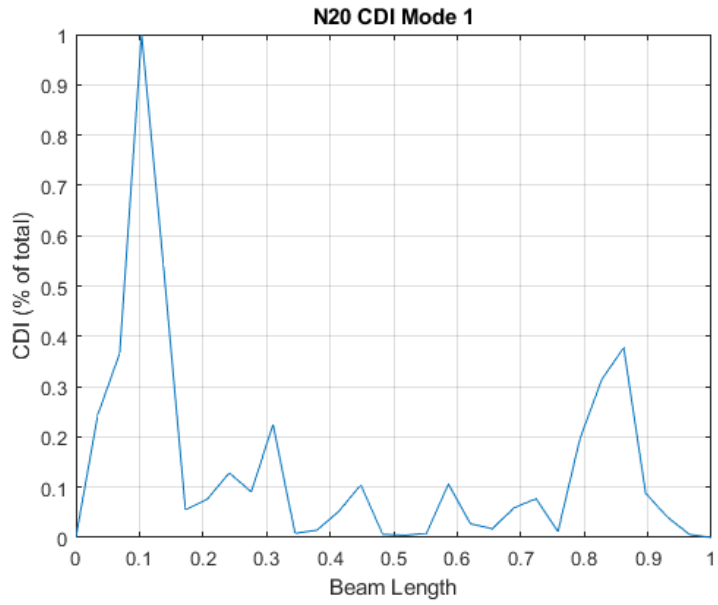


Figure A-36: Beam N20 Mode 1 CDI

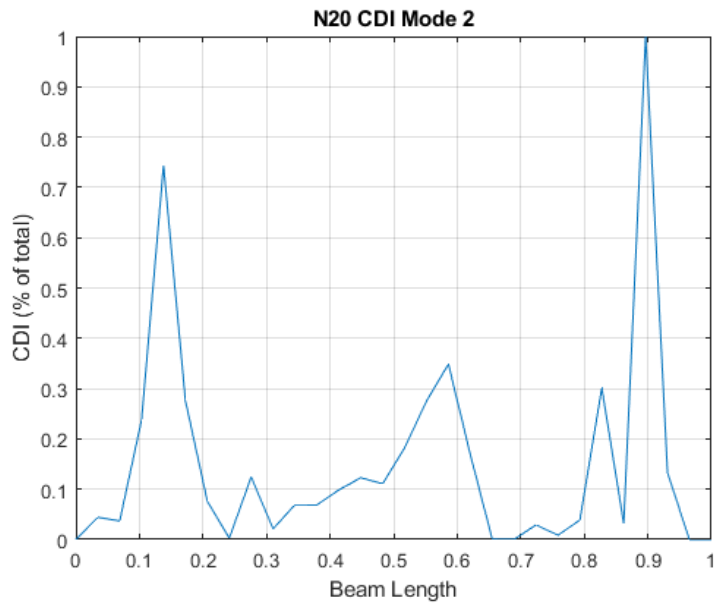


Figure A-37: Beam N20 Mode 2 CDI

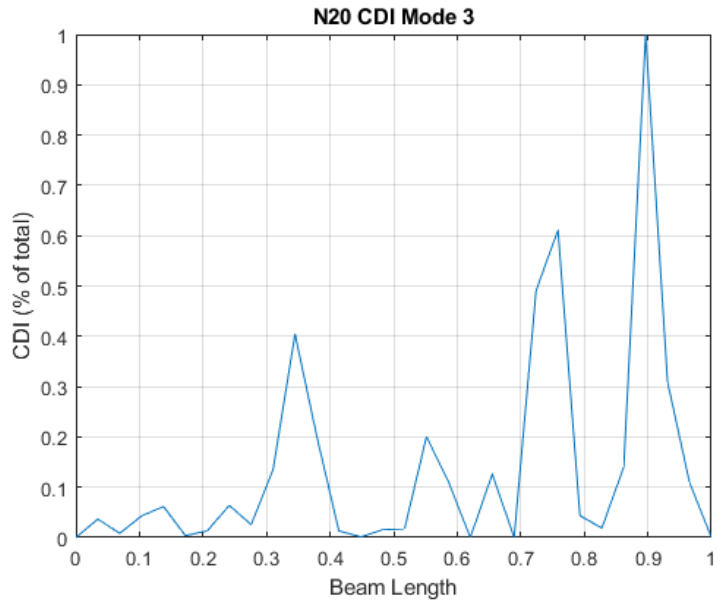


Figure A-38: Beam N20 Mode 3 CDI



Figure A-39: Beam N20 Mode 1 CWT

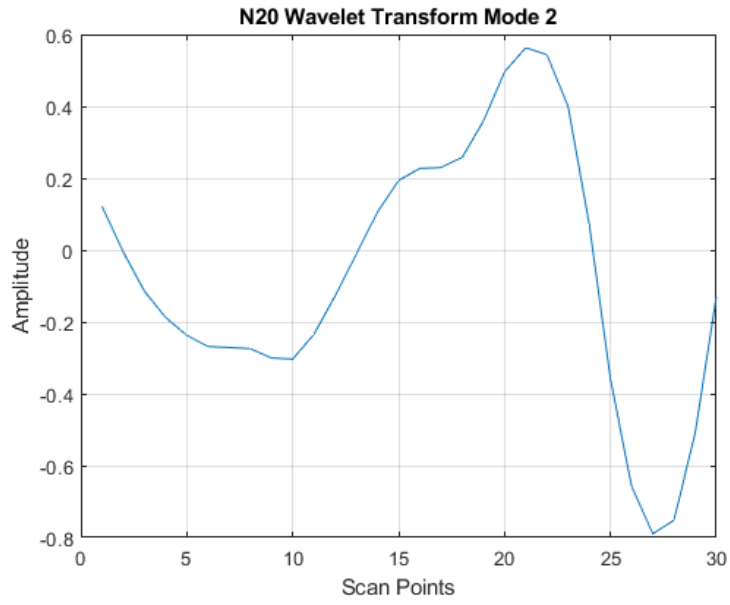


Figure A-40: Beam N20 Mode 2 CWT

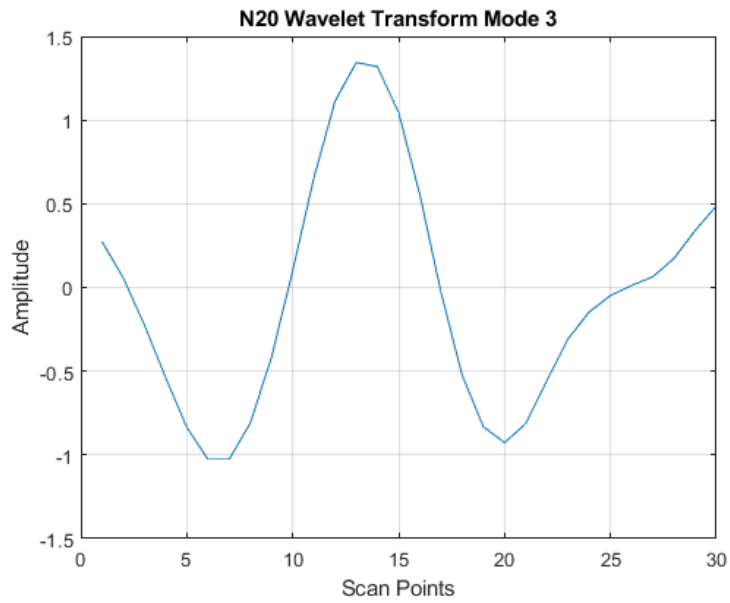


Figure A-41: Beam N20 Mode 3 CWT

APPENDIX B: EXAMPLE MATLAB CODE

```
% mode shape processing
clc;
clear;
close all;

m1_vel=xlsread('N1Scan_31.25_Hz_Fixed.xlsx');

ref_vel=max(abs(m1_vel));

m1_vel=m1_vel/ref_vel;

m1_disp=m1_vel;

% X axis value for mode 1
t1 = linspace(0,1,length(m1_disp));

figure,scatter(t1,m1_disp),grid
title('N1 Mode 1')
xlabel('Beam length')
ylabel('Displacement - Mode 1')

figure,cwt(m1_disp), title('N1 Mode 1')

%%%%%%%%%%%%%%%%%%%%%%%%%%%%%%%%%%%%%%%%%%%%%%%%%%%%%%%%%%%%%%%%%%%%%%%%
%%%%%%%%%%%%%%%%%%%%%%%%%%%%%%%%%%%%%%%%%%%%%%%%%%%%%%%%%%%%%%%%%%%%%%%%
m2_vel=xlsread('N1Scan_346.875_Hz_Fixed.xlsx');

ref_vel=max(abs(m2_vel));

m2_vel=m2_vel/ref_vel;

m2_disp=m2_vel;

% X axis value for mode 1
t2 = linspace(0,1,length(m2_disp));

figure,scatter(t2,m2_disp),grid
title('N1 Mode 2')
xlabel('Beam length')
ylabel('Displacement - Mode 2')
figure,cwt(m2_disp),title('N1 Mode 2')
%%%%%%%%%%%%%%%%%%%%%%%%%%%%%%%%%%%%%%%%%%%%%%%%%%%%%%%%%%%%%%%%%%%%%%%%
%%%%%%%%%%%%%%%%%%%%%%%%%%%%%%%%%%%%%%%%%%%%%%%%%%%%%%%%%%%%%%%%%%%%%%%%
m3_vel=xlsread('N1Scan_962.5_Hz_Fixed.xlsx');
```

```

ref_vel=max(abs(m3_vel));

m3_vel=m3_vel/ref_vel;

m3_disp=m3_vel;

% X axis value for mode 1
t3 = linspace(0,1,length(m3_disp));

figure,scatter(t3,m3_disp),grid
title('N1 Mode 3')
xlabel('Beam length')
ylabel('Displacement - Mode 3')
figure,cwt(m3_disp),title('N2 Mode 3')

h =8/20;% beam length is 8 inches

% Calculating CODS - curvature of operating deflection shape

%%%%%%%%%%%%%%%%%%%%%%%%%%%%%%%%%%%%%%%%%%%%%%%%%%%%%%%%%%%%%%%%%%%%%%%%
% U1 CODS for comparison
m1_vel_U1=xlsread('U1Scan_40.625_Hz_Fixed.xlsx');

ref_vel_U1=max(abs(m1_vel_U1));

m1_vel_U1=m1_vel_U1/ref_vel_U1;

m1_disp_U1=m1_vel_U1;

m2_vel_U1=xlsread('U1Scan_343.75_Hz_Fixed.xlsx');

ref_vel_U1=max(abs(m2_vel_U1));

m2_vel_U1=m2_vel_U1/ref_vel_U1;

m2_disp_U1=m2_vel_U1;

m3_vel_U1=xlsread('U1Scan_962.5_Hz_Fixed.xlsx');

ref_vel_U1=max(abs(m3_vel_U1));

m3_vel_U1=m3_vel_U1/ref_vel_U1;

m3_disp_U1=m3_vel_U1;

% U1 CODS
ydd_u_1_U1=[];

```

```

for i = 2:1:19
    ydd_u_1_U1=[ydd_u_1_U1 (m1_disp_U1(i-1)-2*m1_disp_U1(i)-
m1_disp_U1(i+1))/h^2];
end
ydd_u_1_U1_max = max(abs(ydd_u_1_U1));
ydd_u_1_U1_Fixed = ydd_u_1_U1/ydd_u_1_U1_max;
ydd_u_1_U1=[0 ydd_u_1_U1_Fixed 0];

ydd_u_2_U1=[];
for i = 2:1:19
    ydd_u_2_U1=[ydd_u_2_U1 (m2_disp_U1(i-1)-2*m2_disp_U1(i)-
m2_disp_U1(i+1))/h^2];
end
ydd_u_2_U1_max = max(abs(ydd_u_2_U1));
ydd_u_2_U1_Fixed = ydd_u_2_U1/ydd_u_2_U1_max;
ydd_u_2_U1=[0 ydd_u_2_U1_Fixed 0];

ydd_u_3_U1=[];
for i = 2:1:19
    ydd_u_3_U1=[ydd_u_3_U1 (m3_disp_U1(i-1)-2*m3_disp_U1(i)-
m3_disp_U1(i+1))/h^2];
end
ydd_u_3_U1_max = max(abs(ydd_u_3_U1));
ydd_u_3_U1_Fixed = ydd_u_3_U1/ydd_u_3_U1_max;
ydd_u_3_U1=[0 ydd_u_3_U1_Fixed 0];

%%%%%%%%%%%%%%%%%%%%%%%%%%%%%%%%%%%%%%%%%%%%%%%%%%%%%%%%%%%%%%%%%%%%%%%%

%CODS Calculation

ydd_u_1=[];
for i = 2:1:19
    ydd_u_1=[ydd_u_1 (m1_disp(i-1)-2*m1_disp(i)-m1_disp(i+1))/h^2];
end
ydd_u_1_max = max(abs(ydd_u_1));
ydd_u_1_Fixed = ydd_u_1/ydd_u_1_max;
ydd_u_1=[0 ydd_u_1_Fixed 0];
figure, plot(0:1/19:1,ydd_u_1),grid
title('N1 Mode 1 CODS')
hold on
plot(0:1/19:1,ydd_u_1_U1),grid
legend('N1', 'U1')
xlabel('Beam length')
ylabel('\psi(x) (% of total)')

ydd_u_2=[];
for i = 2:1:19
    ydd_u_2=[ydd_u_2 (m2_disp(i-1)-2*m2_disp(i)-m2_disp(i+1))/h^2];
end
ydd_u_2_max = max(abs(ydd_u_2));
ydd_u_2_Fixed = ydd_u_2/ydd_u_2_max;
ydd_u_2=[0 ydd_u_2_Fixed 0];
figure, plot(0:1/19:1,ydd_u_2),grid
title('N1 Mode 2 CODS')
hold on
plot(0:1/19:1,ydd_u_2_U1),grid

```

```

legend('N1', 'U1')
xlabel('Beam length')
ylabel('\psi(x) (% of total)')

ydd_u_3=[];
for i = 2:1:19
    ydd_u_3=[ydd_u_3 (m3_disp(i-1)-2*m3_disp(i)-m3_disp(i+1))/h^2];
end
ydd_u_3_max = max(abs(ydd_u_3));
ydd_u_3_Fixed = ydd_u_3/ydd_u_3_max;
ydd_u_3=[0 ydd_u_3_Fixed 0];
figure, plot(0:1/19:1,ydd_u_3),grid
title('N1 Mode 3 CODS')
hold on
plot(0:1/19:1,ydd_u_3_U1),grid
legend('N1', 'U1')
xlabel('Beam length')
ylabel('\psi(x) (% of total)')

[Max_1, Loc_1] = max(abs(ydd_u_1));
[Max_2, Loc_2] = max(abs(ydd_u_2));
[Max_3, Loc_3] = max(abs(ydd_u_3));

%%%%%%%%%%%%%%%%%%%%%%%%%%%%%%%%%%%%%%%%%%%%%%%%%%%%%%%%%%%%%%%%%%%%%%%%
%CDI CODS_Notched - CODS un-notched

CDI_N1_Model1 = (ydd_u_1 - ydd_u_1_U1).^2;
CDI_N1_Model1_Max = max(abs(CDI_N1_Model1));
CDI_N1_Model1 = CDI_N1_Model1/CDI_N1_Model1_Max;

CDI_N1_Model2 = (ydd_u_2 - ydd_u_2_U1).^2;
CDI_N1_Model2_Max = max(abs(CDI_N1_Model2));
CDI_N1_Model2 = CDI_N1_Model2/CDI_N1_Model2_Max;

CDI_N1_Model3 = (ydd_u_3 - ydd_u_3_U1).^2;
CDI_N1_Model3_Max = max(abs(CDI_N1_Model3));
CDI_N1_Model3 = CDI_N1_Model3/CDI_N1_Model3_Max;

figure, plot(0:1/19:1,CDI_N1_Model1),grid
title('N1 CDI Mode 1')
xlabel('Beam Length')
ylabel('CDI (% of total)')

figure, plot(0:1/19:1,CDI_N1_Model2),grid
title('N1 CDI Mode 2')
xlabel('Beam Length')
ylabel('CDI (% of total)')

figure, plot(0:1/19:1,CDI_N1_Model3),grid
title('N1 CDI Mode 3')
xlabel('Beam Length')
ylabel('CDI (% of total)')

%%%%%%%%%%%%%%%%%%%%%%%%%%%%%%%%%%%%%%%%%%%%%%%%%%%%%%%%%%%%%%%%%%%%%%%%
% Wavelet Analysis

```

```
c1 = cwt(ydd_u_1, 1:128, 'db4');  
figure  
plot(c1(10,:));  
title('N1 Wavelet Transform Mode 1')  
grid  
xlabel('Scan Points')  
ylabel('Amplitude')
```

```
c2 = cwt(ydd_u_2, 1:128, 'db4');  
figure  
plot(c2(10,:));  
title('N1 Wavelet Transform Mode 2')  
grid  
xlabel('Scan Points')  
ylabel('Amplitude')
```

```
c3 = cwt(ydd_u_3, 1:128, 'db4');  
figure  
plot(c3(10,:));  
title('N1 Wavelet Transform Mode 3')  
grid  
xlabel('Scan Points')  
ylabel('Amplitude')
```